UNIVERSITÀ DEGLI STUDI DI PADOVA

Dipartimento di Fisica e Astronomia “Galileo Galilei”

Master Degree in Astrophysics and Cosmology

Final Dissertation

Polarized X-rays from magnetars: IXPE observations of AXP 4U 0142+61

Thesis supervisor
Prof. Roberto Turolla
Thesis co-supervisor
Dott. Roberto Taverna

Candidate
Eleonora Andreis

Academic Year 2022/23

Abstract

In this work, we analyze the IXPE observations of the polarized X-rays coming from the AXP 4U 0142+61. Firstly, we briefly introduce neutron stars, then we take a deeper look into the magnetar model: the twisting of the magnetosphere and its consequences, the detected emission and its possible explaining models, the polarization of magnetar radiation and the role it plays in understanding to a deeper level the various mechanisms that are at work. The effects that arise due to the presence of the huge magnetic field of these sources, such as vacuum birefringence and mode switching, are taken into account. Lastly, we analyze the data received from the AXP 4U 0142+61 and we try to fit them with the various models that we computed. The latter are derived dividing the star in a 10×10 grid and assigning to each patch a temperature. We take different values for the amount of twist of the star $\Delta\phi$ and for the velocity of particles flowing in the corona β, assuming a unidirectional flow of electrons which will undergo resonant Compton scattering in the magnetosphere, implemented using a Monte Carlo technique. Then, we also account for the different angles that the magnetic field of the star makes with its rotation axis, ξ, and the different viewing angles of our source, χ. Furthermore, we consider two emission models for the star: a condensed surface with either free or fixed ions. In the end, we obtain the best fit value of all the aforementioned parameters and the value of the Polarization Degree (PD) and Polarization Angle (PA) of the aforementioned source.

Contents

Chapter 1

Introduction

The Imaging X-ray Polarimetry Explorer (IXPE) [1] is a NASA-ASI (Agenzia Spaziale Italiana) mission announced on 3 January 2017 and launched on 9 December 2021. It is the first space telescope entirely devoted to polarimetry observations in the soft X-ray (2–8 keV) energy band, and it has already observed more than 40 X-ray sources, including supermassive black holes, pulsar wind nebulae and neutron stars.

Magnetars are a class of isolated neutron stars (INSs), first divided into Anomalous X-ray Pulsars (AXPs) and Soft-Gamma Repeaters (SGRs), believed to be powered by the decay of their enormous magnetic field [2]; they are of particular interest for IXPE observations. They are the strongest magnets we know in the universe, since the magnetic field inferred from their spin period $P \sim 2$–12 s and their period derivative $\dot{P} \sim 10^{-13}$–10^{-11} $\mathrm{s\,s^{-1}}$ is $B \sim 10^{14}$–10^{15} G (the strongest magnetic field produced on Earth is $\sim 4.5 \times 10^5$ G). They are characterized by a persistent X-ray luminosity $L_X \sim 10^{31}$–10^{36} $\mathrm{erg\,s^{-1}}$, higher than their spin-down one, and by an intense bursting activity with different luminosities ($L_X \sim 10^{39}$–10^{47} $\mathrm{erg\,s^{-1}}$) and timescales (few seconds to several hundreds), from the short bursts up to the hyperenergetic giant flares. Their persistent spectra in the soft X-ray range (0.5–10 keV) are usually fitted by a two-component model, with either a blackbody superimposed to a powerlaw, for most magnetars, or two blackbodies at different temperatures, in particular for the so-called transient magnetars. These sources are characterized by outbursts, i.e. a sudden increase of the X-ray flux by a factor ~ 10–10^3 over their quiescent level, that can last up to some hours and during which the emission of short bursts can occur. They are usually faint sources, an can be detected only during their outbursts periods. The internal magnetic field of magnetars is believed to be even higher than the external one, $B \gtrsim 10^{16}$ G, and it is thought to deform and yield the magnetar surface, transferring a toroidal component to the otherwise dipolar external magnetic field, making the magnetic field lines to twist up, with currents flowing along them in the so-called twisted magnetosphere. The photons coming from the cooling surface of the magnetar, believed to give rise to the thermal component of the spectra observed below 10 keV, undergo resonant Compton scattering (RCS) onto the charged particles in the magnetosphere, giving rise to the powerlaw component in the soft X-ray. This RCS model was derived to explain spectral observations; however, even if it is able to account for the powerlaw component of the spectrum, it does not put any constraint on the mechanisms responsible for the surface emission. Up to now, magnetars were studied only through spectral measurements (since polarization observations were not able to give significant measurements), but the latter are degenerate with respect to many of the parameters used to model magnetar persistent emission, e.g. the underlying emission model, the magnetic field topology and the geometry (the angle that the line of sight and the magnetic field axis make with the rotation axis, χ and ξ respectively). X-ray polarimetry, instead, is going to play a fundamental role in disentangling the geometry and magnetospheric topology of magnetars, as well as their surface emission model. In fact, radiation coming from such strong magnetic sources is expected to be substantially (linearly) polarized in two normal modes: the ordinary (O) and extraordinary (X) mode, having the polarization electric vector either parallel or perpendicular, respectively, to the plane of the (local) magnetic field and the photon direction; besides depending on the orientation and strength of the star magnetic field, the degree of polarization observed from these sources depends as well on the geometry of the emission region and on the physical processes photons undergo at the emission and along their path from the source to infinity [3]. The observed polarization properties are generally expected to be different from those at the surface of the star, where radiation is emitted. In fact, since they do depend on the magnetic field orientation, and the latter is particularly tangled near the magnetar surface, polarization from different surface regions would cancel each other, resulting in a low polarization degree. However, in the presence of strong magnetic fields the vacuum around the star is expected to become birefringent, as predicted by QED; this would make the photons to retain their initial polarization mode, up to the adiabatic radius (for typical magnetar parameters $r_a \sim 150$ stellar radii). Therefore, a high polarization degree value may be the first indirect evidence of the birefringence of the vacuum [4].

The aim of this thesis is to better characterize the underlying emission model of the magnetar AXP 4U 0142+61 doing a phase-dependent analysis of the data collected from IXPE observations of the source in February 2022, which were analyzed by Taverna et al. [5] in the framework of the RCS model, and were successfully fitted by a model characterized by the emission from an equatorial belt in a condensed state further reprocessed by RCS in the magnetosphere. This is carried out computing different models for the source surface emission: a condensed iron surface in the fixed/free ions limit characterized by a hotter equatorial belt or by antipodal spots on the surface of the star, at different temperatures and with different values for the parameters $\Delta\phi$, β, χ, and ξ. The work is organized as follows: in the second chapter a brief introduction to the main features and types of neutron stars is found; the third chapter is devoted to the details of the magnetar model and to the spectral observations performed so far; in the fourth chapter we present the data extraction process (comprising also a brief description of the IXPE polarimeter), the computation of the synthetic models and the fit of the real data with the latter; the fifth chapter is dedicated to the discussion and the analysis of the obtained results; conclusions follow in the last chapter.

Chapter 2

Neutron stars

2.1 Formation and main properties

Stars with an initial mass of $M \gtrsim 8M_\odot$ undergo a core-collapse supernova event at the end of their life. Like the other stars, at the beginning of the main-sequence stage, they start burning hydrogen, passing then to helium, carbon, neon, and finally oxygen, creating different concentric shells where the different elements are burnt. Each of these successive burning stages is possible thanks to the gravitational contraction of the star which enables the ignition of the next element burning by raising the temperature. After the oxygen burning, ^{28}Si and ^{32}S are produced but the latter has a too high potential barrier and can not be burnt via nuclear fusion; so, through successive α-capture processes the iron peak is reached and iron, nichel and cobalt are synthesized. These elements have the maximum binding energy per nucleon and a supply of energy is required to synthesize heavier elements. Although the star keeps contracting, trying to increase the temperature and burn these elements, the gravitational force is too large to be balanced by the degenerate electron pressure. The latter leads to the formation of white dwarfs in lighter stars, so that when the mass of the core exceeds the Chandrasekhar limit $M_{\text{core}} > M_{ch}$ [1] the star cannot end its life as an object supported by electron degeneracy pressure. As a consequence, the temperature of the star keeps increasing and highly energetic photons are produced which photodissociate iron. Due to the collapse, the density increases to the point where not only electrons are degenerate but also neutrons and protons. Electron capture, or inverse β decay, $p + e^- \to n + \nu$, becomes possible when the increased Fermi energy of the electrons balances the mass defect, and so nuclei are more and more enriched by neutrons. Once the nuclear drip line is overcome, neutrons start to drip out of the nuclei. Neutrinos are also formed, but they immediately fly away, subtracting energy and favoring the collapse. After the explosion only the bare core of the star is left, which collapses under its own weight; if the mass is not too high the neutron-degeneracy pressure is able to restore hydrostatic equilibrium forming a neutron star, otherwise a black-hole is formed.

Neutron stars (NSs) have typical values of radius $R \simeq 10$ km, and mass $M \simeq M_\odot$ for a core density $\rho_{\text{core}} \simeq 10^{15}$ g/cm^3. The Schwarzschild radius $R_S = 2GM/c^2$ of such an object is ~ 3 km, so comparable to the typical radius of neutron stars. Therefore neutron stars are indeed extremely compact objects and we have to take into account

---

[1] M_{ch} is the Chandrasekar mass: the maximum mass that a spherical equilibrium configuration can reach if it is supported by the degeneracy pressure of the electron gas alone, so is the maximum mass of a white dwarf

the general-relativistic effects that arise [6]. They also rotate very fast: to give an idea of the order of magnitudes of the spin of these objects, one can assume the collapse of a Sun-like star into a neutron star. Assuming that the angular momentum is conserved $L = I\omega = I_{NS}\omega_{NS}$, with $I = (2/5)MR^2$ the moment of inertia, the following holds:

$$M_* R_*^2 \omega_* = M_{NS} R_{NS}^2 \omega_{NS}. \tag{2.1}$$

Substituting $\omega = 2\pi/P$, results

$$P_{NS} = P_* \frac{R_{NS}^2}{R_*^2} \tag{2.2}$$

and, replacing with typical values, with the rotation period of the progenitor star $P_* \approx 10^5$–10^6 s, we obtain $P_{NS} \approx 10^{-4}$ s, which is just an estimate, typical period of neutron stars are higher. Moreover, NSs are highly magnetized, in fact, they are the strongest magnets we know in the universe. Once again order of magnitude, supposing that also the magnetic flux is conserved during the core-collapse

$$B_* R_*^2 = B_{NS} R_{NS}^2, \tag{2.3}$$

with $B_* \simeq 10^2$ G, we find $B_{NS} \approx 10^{12}$ G, which is indeed very huge compared to the magnetic fields we can measure in the Solar system.

2.2 The neutron star zoo

We restrict our analysis to the first order contribution of the magnetic field, the dipole. As it can be seen in figure 2.1, $\vec{\mu} \parallel \vec{B}_d$ is the magnetic axis, $\vec{\Omega}$ is the rotation axis and ξ is the angle between them (assumed to be constant with time), while χ is the angle between the line of sight (LOS) and $\vec{\Omega}$, and $\psi = \Omega t$ is the rotational phase. So we have: $\vec{\mu} = \mu(\sin\xi\cos\psi, \sin\xi\sin\psi, \cos\xi)$ and we define the module of the magnetic moment as $\mu = B_p R_{NS}^3$, where B_p is the polar magnetic field. The Larmor formula gives us the power lost for a rotating dipole:

$$W = \frac{2\ddot{\mu}^2}{3c^3}, \tag{2.4}$$

where the dot denotes a time derivative. Substituting it in $\dot{E}_K = I\Omega\dot{\Omega} = -W$, where E_K is the kinetic rotational energy, we obtain the evolution of the star spin with time:

$$\dot{\Omega} = -\frac{2}{3Ic^3} B_p^2 R_{NS}^6 \sin^2\xi\,\Omega^3 = -A\Omega^3, \tag{2.5}$$

where $A = -(2/3Ic^3)B_p^2 R_{NS}^6 \sin^2\xi$. So the rotation velocity of the NS undergoes a secular decrease and integrating the latter equation from the neutron star birth to date, it results:

$$\frac{\dot{\Omega}}{\Omega^3} = -A \quad \Longrightarrow \quad \frac{1}{2\Omega_0^2} = \frac{1}{2\Omega^2} - A(t - t_0), \tag{2.6}$$

where the subscript 0 refers to the new-born neutron star. Supposing $t \gg t_0$ we have $\Omega_0 \gg \Omega$, thus we can neglect the terms Ω_0^{-2} and t_0, so the last equation becomes:

$$\Omega^{-2} \approx 2At \quad \Longrightarrow \quad \Omega \propto t^{-1/2}, \tag{2.7}$$

known as the spin-down frequency. From $P = 2\pi/\Omega$ and equation (2.7) it follows:

$$P^2 = \frac{4\pi^2}{\Omega^2} = \frac{16\pi^2}{3c^3 I} B_p^2 R_{NS}^6 \sin^2(\xi) t = A8\pi^2 t. \tag{2.8}$$

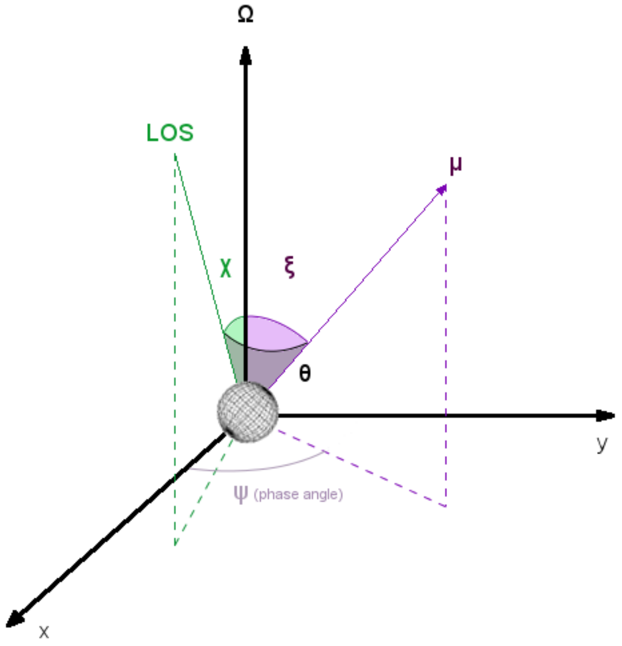

Figure 2.1: Geometry of the neutron star. Image taken from [7]

In the latter equation we can substitute $A = -\dot{\Omega}/\Omega^3$ and, since $\mathrm{d}P/P = -\mathrm{d}\Omega/\Omega$, we can define the characteristic time as $t_{\text{char}} \approx P/2\dot{P}$. In addition, from equation (2.8) it can be seen that

$$P\dot{P} = -(4\pi)^2 \frac{\dot{\Omega}}{\Omega^3} = \frac{8\pi^2 B_p^2 R_{NS}^6 \sin^2 \xi}{3Ic^3}. \tag{2.9}$$

From the latter expression we can estimate the spin-down magnetic field:

$$B_p = \sqrt{P\dot{P}} \sqrt{\frac{3Ic^3}{8\pi^2 R_{NS}^6 \sin^2 \xi}} \approx \frac{6 \times 10^{19}\ \mathrm{G}}{\sin \xi} \sqrt{P\dot{P}}. \tag{2.10}$$

We can hence classify all the observed NSs as functions of their values of P and $\dot{P}$ in the so-called $P - \dot{P}$ diagram, where we have P on the horizontal axis and $\dot{P}$ on the vertical axis. Given that both B_p and the characteristic age depend on P and $\dot{P}$, we can draw constant magnetic field and characteristic time lines in the $P - \dot{P}$ diagram, as it can be seen in figure 2.2. Therefore, we can follow the evolution of NSs evolving with constant B, and NSs with similar characteristic age can be distinguished. In this diagram we can distinguish various types of neutron stars, which are also set apart by their different observational properties.

- **Rotation-powered pulsars**: These sources emit in a wide band of frequencies, from radio to optical and from X- to γ- rays; they are fueled by the rotational energy radiated away by the co-rotating magnetic field as the pulsar spins down. They have periods from few seconds to several seconds [9].
- **Accretion-powered pulsars**: They are typically part of a binary system, with hot-spots on the surface, responsible for the X-ray pulsed emission and heated by the flow of the accreting matter from the binary companion. The pulsation is due to the rotation of the star and hence to the change in the visible area of these hot-spots. Their spin behavior is unpredictable, alternating periods of spin-up and

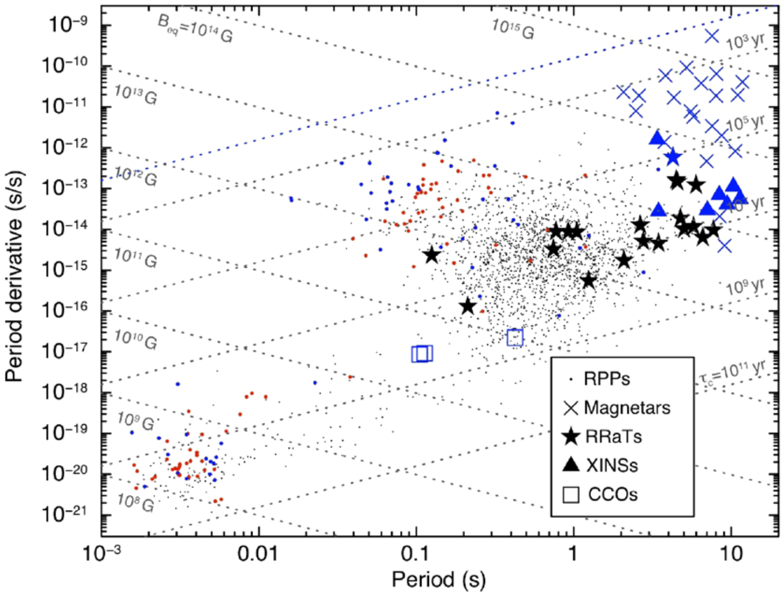

Figure 2.2: Example of a $P - \dot{P}$ diagram. The dotted lines represent constant magnetic field and characteristic time. Image taken from [8].

spin-down and, eventually, glitches. Among these sources, there are also pulsars with periods below 20 milliseconds, called millisecond pulsars [9].

Other objects are also characterized by the fact that no accretion phenomena from companion stars, stellar winds or accretion disks have been observed for them, which led to name them as Isolated Neutron Stars (INSs). These are:

- **RRaT (Rotating Radio Transient)**: They are a particular type of INSs which exhibit an extreme variability in their emission, up to the point where they can become silent for months or even years [10].
- **XDINSs (X-ray Dim Isolated Neutron Stars)**: There are only 7 known objects of this type (The Magnificent Seven), which emit thermal radiation in the X-ray energy band and do not seem to have radio counterparts. They exhibit discrepancies between kinematic/cooling ages and spin-down ones; the former lie between ∼ 0.1–1 Myr, while the latter are in the range ∼ 1–4 Myr. The inferred strength of their dipole field is $\sim 10^{13}$–10^{14} G. There are various model to explain their emission and evolution, in the main one XDINSs would be aged magnetars, with a magnetic field that has reached the end of the Hall-phase (Hall attractor) [11][12].
- **CCO (Central Compact Objects)**: They are at the center of core-collapse supernova remnants and they are still associated with them; they are hence young NSs with a rather weak dipole field. Maybe the magnetic field is buried deep beneath the material accreted from the remnant. So far no radio signal has been detected. It is difficult to measure their period, so it is even more difficult to measure its derivative [13].
- **Magnetars**: These objects are powered by the decay of their incredibly huge magnetic field $\sim 10^{14}$–10^{15} G, which is able to drive also their burst activity (short

bursts, intermediate and giant flares). Their periods lie in the interval 2–12 s. In these sources the magnetic field approaches and exceeds the quantum critical field strength, $B_Q = m_e^2 c^3/(e\hbar) = 4.4 \times 10^{13}$ G, at which the cyclotron energy equals the electron rest mass. Therefore the physical processes are deeply influenced and some additional effects occur, which do not take place in the low-field limit [14].

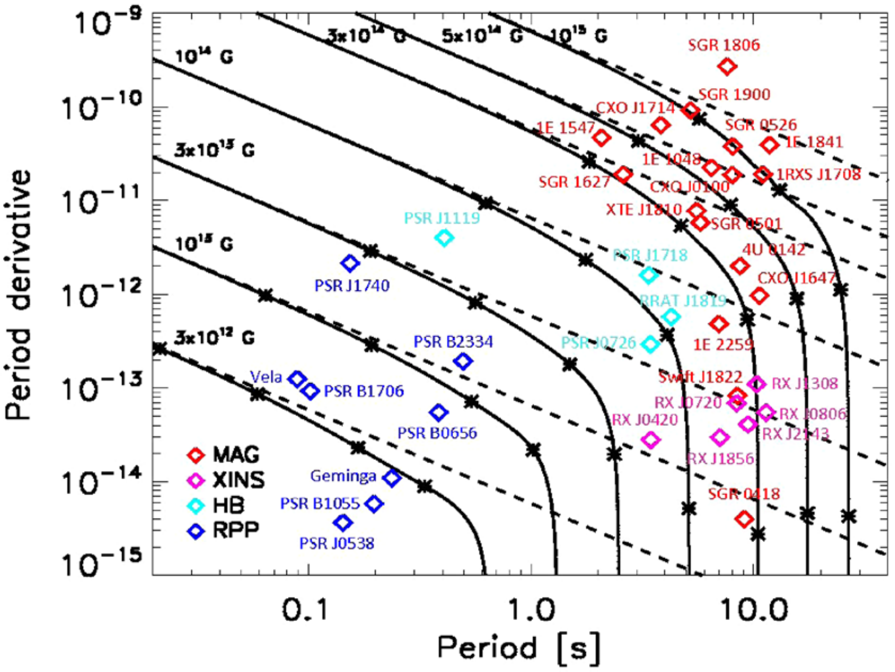

Figure 2.3: Evolution of INSs in the $P - \dot{P}$ diagram, with different initial magnetic fields. Asterisks along the track mark the real ages of the source (10^3, 10^4, 10^5, 5×10^5 yr), while the dashed lines give the tracks followed if B was constant. Image taken from [15].

There could be evolutionary links among the different classes: for example, XDINSs could be aged, worn out magnetars. In fact, all the birthrates of these neutron stars, when summed together, cannot exceed the Galactic core-collapse supernovae rate. This led to the search for a unifying model which could explain each neutron star as a different manifestation of the same underlying physics, the so-called "Grand Unification of Neutron Stars" (GUNS) [16]. In this scenario, the evolution, and hence the properties, of an isolated neutron star are determined by its parameters at birth – for example, mass, period, and magnetic field. The latter has particular relevance in the construction of this model. As the field evolves (even more so if it is a strong one), it decays, hence the path of the star in the $P - \dot{P}$ diagram, after $\approx 10^5$ yrs, deflects towards the bottom, as reported in figure 2.3 [15]. Therefore, the period of the star increases only up to a certain point, determined by the crust resistivity, the initial magnetic field, and the mass of the star. As a consequence, stars that are born as magnetars with an initial field of a few 10^{14} G might evolve into XDINSs [17].

Chapter 3

Magnetars

3.1 Definition and main properties

Magnetars were first divided into anomalous X-ray pulsars (AXPs) and soft-gamma repeaters (SGRs). The former, as the name says, were discovered as X-ray pulsars with a rather high luminosity ($\sim 10^{34}$–10^{36} erg/s) in the soft X-ray range (0.5–10 keV); the latter, instead, are characterized by the emission of bursts in the hard X-ray/soft γ-ray range. They seemed two classes of distinct and different objects, but they share some observational properties [14]:

- they are isolated neutron stars, i.e. they do not belong to a binary system;
- their persistent (non-bursting) emission is very similar both in the soft and in the hard (10–100 keV) X-ray bands;
- the persistent X-ray luminosity normally exceeds the rotational energy loss rate, $L_X \gg \dot{E} \sim 4 \times 10^{46}\, \dot{P}/P^3\ \mathrm{erg\,s^{-1}}$;
- they are observed to pulsate at similar spin periods $P \sim 2$–12 s and with similar spin-down rates $\dot{P} \sim 10^{-13}$–10^{-11} s s^{-1}, which lead to enormous magnetic fields $B \sim 10^{14}$–10^{15} G;
- also AXP were seen to exhibit bursting activity resembling the bursts of SGR [18].

This led to the unification of these two sources under the category of magnetars, in fact the dissipation and decay of an ultra-strong magnetic field is able to power their persistent X-ray emission [2][19], which can not be sustained by the rotational energy loss rate (believed to fuel standard pulsars). Such huge magnetic fields are believed to power also the hyperenergetic ($\sim 10^{44}$–10^{47} erg/s) giant flares. The range of periods (2–12 s) magnetars exhibit is incredibly narrow with respect to the one of radio pulsars, sweeping from 1.4 ms to 8.5 s, and the one of X-ray binaries, varying between milliseconds and hours. Their period derivatives are clustered in the range $\dot{P} \sim 10^{-13}$–10^{-11} s s^{-1}, which means a large secular spin-down rate, which is observed to be quite irregular.

All magnetars exhibit variability in their persistent X-ray emission, but it is more extreme in some sources, known as transient magnetars (see e.g. [20]). Their flux upswings by a factor ≈ 10–1000 with respect to the quiescent state in only a few hours, along with the emission of short bursts. This phases of enhanced emission last approximately 1 year and are usually called outbursts. The flux then gradually diminishes, the pulse profile simplifies and the spectrum softens in a different way for each source and even for distinct outbursts of the same source. Among these transient magnetars, two sources (SGR 0418+5729 [21] and Swift J1822.3-1606 [22]) were found to possess an unusually low magnetic field $B \leq 10^{13}$ G, which is a typical value of radio pulsars. Both of them have a large characteristic age, show few and soft bursts, and have a low persistent luminosity in quiescence. However, the X-ray spectrum of SGR 0418+5729 exhibited a proton cyclotron absorption line, which led to an inferred (local) magnetic field ranging from 2×10^{14} G to more than 10^{15}, much higher than the one derived from its timing parameters [23].

3.2 Birth and evolution

3.2.1 Formation of a magnetar

Magnetars are believed to descend from massive stars, at the far end of the mass distribution of OB stars. In fact, some SGRs and AXPs are found in young clusters of massive stars, see for example [24]. If we consider the standard evolutionary models, the progenitors with masses $\sim$ 20–45$M_\odot$ for the most part should have given rise to black holes [25].

There are two main mechanisms that can explain the formation of such an enormous magnetic field. Thompson and Duncan [19] hypothesized that in the early, highly convective stages of the proto-neutron star, its magnetic field could be amplified by an intense dynamo action. Two types of dynamo can be produced by rotation and convection in an astrophysical plasma: one is driven by the differential rotation, called ω dynamo, while the other (the α dynamo) arises from the coupling of convective motions and rotation. To guarantee an efficient convective mixing in the proto neutron stars, since both dynamos are present and they operate at low Rossby numbers[1], the initial spin period must be short [2]. The rapidly spinning and collapsing stellar cores lead to a highly-energetic supernova explosion [26], due to the strong magnetic coupling, which is able to transfer a great fraction of the rotational energy, $E_{rot} \sim 3 \times 10^{52}\ (P/1\ \mathrm{ms})^{-2}$ erg, to the ejecta. Despite the search for magnetars associated with above-average supernova events, no observational feature has been found yet [27]. Maybe gravitational waves can carry away this rotational energy if $B \gtrsim 10^{16}$ G, and they do not interact with matter [28]. Another possibility is that magnetars are formed in a very close binary system, where the core of the rapidly rotating neutron star would be accelerated by tidal synchronization [29]. An example of this may be given by the magnetar CXO J164710.2−455216, which was recently associated with Wd1-5[2][30]. The latter would be ejected from the massive binary when the progenitor of the magnetar exploded. The progenitor's mass in this scenario would decrease through intense stellar wind activity when entering a Wolf-Rayet phase, and common envelope evolution would prevent the spin-down of its core. Therefore this formation process would simultaneously provide the spark that will ignite the convective dynamo and bring the mass back into the neutron star formation range, in place of a black hole. The other theory states that magnetic fields of neutron stars were already present at birth and they would be amplified during the collapse of the core through magnetic flux conservation, $B \propto R^{-2}$. This is the fossil field scenario [31]. Using this model $\sim$ 25 magnetars would be formed from high-field

---

[1] The Rossby number is usually defined as the ration between Coriolis and inertial forces; here it is calculated as the ratio between the rotation period of the star and the local convective turnover time.

[2] A star in the globular cluster Westerlund1.

core-collapse supernovae. Nowadays, considering the increasing population of magnetars and the discovery of latent magnetars among radio pulsars [32], the prediction of the fossil field scenario seems to fall short of observations. Moreover, magnetars may be also related to both short and long GRBs [33]. A magnetar created from coalescence in a double-degenerate binary (or accretion-induced collapse of a white dwarf) may explain short GRBs, while the long ones may arise in a magnetar created from coalescence in a core-collapse supernova [34]. Probably magnetars are not entirely formed through one process, more than one mechanism could be at work.

3.2.2 Evolution of the internal field

The structure and the strength of the internal magnetic field are poorly constrained by observations. Having to sustain the magnetar emission and also the greatly energetic flares, the internal magnetic field has to be strong enough, approaching $\sim 10^{16}$ G [35], and its topology has to allow the outflowing of the magnetic energy; it most likely consists of both poloidal and toroidal components [36]. It is not certain where the magnetic field resides in the star. According to where its supporting (super)currents are located, it can lie predominantly in the crust or it can be diffused in the whole star. In the former case, we talk about a "crustal" field, in the latter about a "core" field. Therefore, in the most general case, the internal magnetic field of a neutron star will be generated by a superposition of currents both in the crust and in the core. Based on the type of neutron star that we are looking at the importance of these fields will be different [37]. In the case of a magnetar, having to significantly decay over a timescale of $\sim 10^3$–10^5 yrs, a crustal field seems to be the most probable configuration [38].

The evolution of the magnetic field in a neutron star proceeds through a series of quasi-equilibrium states alternated by hydrodynamic motion in its liquid core and release of elastic stresses in the crust; it evolves according to [39]:

$$\frac{\partial \vec{B}}{\partial t} = -\nabla \times \left(\frac{c^2}{4\pi\sigma} \nabla \times \vec{B} \right) + \nabla \times \left(-\frac{\vec{j}}{n_e e} \times \vec{B} \right) + \nabla \times (\vec{v}_a \times \vec{B}). \tag{3.1}$$

Each term on the right-hand side represents a different effect:

1. The first one describes the Ohmic diffusion of the magnetic field. In the core, where all particles are degenerate, the conductivity σ (defined from the current density $\vec{j}$ and the electric field $\vec{E}$, $\vec{j} = \sigma \vec{E}$) is large. This leads to a characteristic time of $t_{\text{Ohmic}} \sim 2 \times 10^{11} (L_{\text{km}}/T_8)^2 (\rho/\rho_{\text{core}})^3$ yr [39], where $\rho_{\text{core}} = 2.8 \times 10^{14}$ g cm^{-3} is the density of the core, $L_{\text{km}} = L/(1 \text{ km})$ is the lengthscale over which the field is varying and $T_8{=}T/(10^8$ K) is the temperature. Clearly, the decay time would be shorter if currents were confined to the crust [40].

2. The second term accounts for the advection of the field by Hall drift: the electron fluid carries the magnetic field and it drifts with respect to the ions, with velocity $\vec{v}_e = -\vec{j}/(n_e e)$. This term is non-dissipative, but it can change the field structure on a timescale $t_{\text{Hall}} \sim 5 \times 10^8 (\rho/\rho_{\text{core}}) L_{\text{km}}^2 / B_{12}$ yr, where $B_{12} = B/(10^{12}$ G). The Hall term is inherently conservative. However, it highly amplifies the dissipation of energy in the first 10^6 yrs of a neutron star life, since it drives the magnetic field towards smaller spatial scales, where dissipation is faster [37]. Its main effect though, for fields $B \gtrsim 10^{14}$ G, is to transfer part of the magnetic energy from large to small scales and to couple the poloidal and toroidal magnetic field. Even

if the latter is zero at first, it is quickly created. Instead, if the toroidal component is stronger, it provokes the development of current sheets where the dissipation is strongly enhanced. It has been pointed out by Goldreich & Reisenegger [38] that the Ohmic dissipation rate of the field might be increased by a turbulent cascade to small scales triggered by the nonlinear Hall term. A recent simulation of electron MHD turbulence confirmed this "Hall cascade" [41].

3. The last term describes ambipolar diffusion, that involves a drift of the electron-proton fluid, transporting the magnetic field, with respect to the neutrons. At variance with the Hall term, ambipolar diffusion is dissipative and this makes the core and the deep crust of a magnetar to heat up; this might be the underlying mechanism of their persistent X-ray emission [42].

In magnetars these three effects have different relevance. During their active lifetime ambipolar diffusion is of little importance in magnetar cores (in the crust it is quenched by the absence of convective motions) [43]. Since magnetar activity is due to the field evolution/decay, it must be governed by Hall and Ohmic diffusion, which take place in the crust. Given that this two effects are strongly density- and temperature-dependent, a self-consistent study of the evolution of the magnetic field has to be accompanied by a detailed modelling of the thermal evolution of the neutron star, and vice versa. So the cooling and the induction equation of the magnetic field must be solved simultaneously. A solution to this problem, accounting for both the Ohmic diffusion and the Hall drift, has been given by De Grandis et al. [44]. The magnetic field of magnetars is subject to sudden changes, for example when the crust yields [45]. Stresses in the crust will build up due to the Hall drift of the magnetic field, since the crust has a finite shear modulus μ, and if the elastic stress is exceeded the lattice will yield. This might be causing magnetar bursts [46].

3.3 Twisted magnetosphere

3.3.1 Formation of the twist

As we said when talking about the evolution of the internal field of magnetars, sooner or later a toroidal component builds up, at least of the same order as, or even stronger than, the poloidal one [47]. This brings to the development of a strong deformation of the neutron star surface, that will produce a yield of the crust when the magnetic stress exceeds the crust tensile strength. The crustal platelets will drift due to the effect of the toroidal part of the field. This reflects on the external magnetic field, hence on the magnetar magnetosphere, as it will differ from the commonly assumed dipole. The field lines that are anchored on the displaced crustal patches will twist [48], injecting an electric current into the magnetosphere, since the twisted field is non-potential and hence requires supporting currents. We now see more in detail how this mechanism works.

In a magnetar, the internal field can exceed 10^{15} G [46] and is believed to be globally twisted, so it is strong enough to transfer this twist to the external field lines. Consider a flux tube that has a non-zero toroidal component in the crust and a vanishing one outside the star. The magnetic stresses overcome the crustal tensile strength and cause the crust to yield. The applied forces then drive horizontal displacements of the crustal patches, parallel to the equipotential surfaces. This means that the magnetically-stressed surface elements tend to rotate by an angle $\Delta\phi$ [48]. Given that the external magnetic field

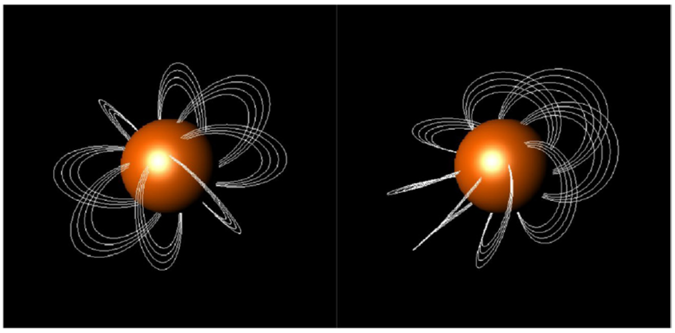

Figure 3.1: In the left panel we can see a pure dipole magnetic field, while in the right panel a globally twisted dipolar field configuration is shown. Image taken from [8]

lines are anchored to the crust, the net effect of the magnetically-induced torsional displacement of the surface layers will be the twisting of the external field, due to the transmission of the internal magnetic helicity outwards. Therefore the external field, even if dipolar at the beginning, will develop a toroidal component, a twist, restricted to the field lines whose footpoints are on the shifted layer. As a consequence, to sustain the non-potential field, currents will flow also along the closed field lines [8], as opposed to what happens normally in radio pulsars, where the Goldreich-Julian currents flow only along the open field lines, since the magnetic field is non-potential there. Of course this displacement of the crust, and consequently the twist of the magnetosphere, will be localized [49]. However when studying the characteristic of the magnetar emission a globally twisted magnetosphere, depicted in figure 3.1 and first proposed in [50], is chosen most times, for simplicity.

The globally twisted magnetosphere model assumes an initial external dipole magnetic field that is then sheared due to the crustal displacements. To understand better the behaviour of the magnetic field, following [8], we start by writing the force-free condition $(\vec{\nabla} \times \vec{B}) \times \vec{B} = 0$, derived from the momentum equation in a low-density plasma and the Ampère-Maxwell equation. If we use a flux function $\mathcal{P}$ to represent the poloidal component and a spherical coordinate system (r, θ, ϕ), then we can write an axisymmetric magnetic field in its most general form:

$$\vec{B} = \frac{\vec{\nabla}\mathcal{P}(r,\theta) \times \vec{u}_\phi}{r \sin\theta} + B_\phi(r,\theta)\vec{u}_\phi \tag{3.2}$$

where B_ϕ is the toroidal component and $\vec{u}_\phi$ is the unit vector in the ϕ direction. Furthermore, we can write the explicit expression of the magnetic field exploiting the force-free condition:

$$\vec{B} = \frac{B_p}{2}\left(\frac{r}{R_{NS}}\right)^{-p-2}\left[-f', \frac{pf}{\sin\theta}, \sqrt{\frac{Cp}{p+1}}\frac{f^{1+1/p}}{\sin\theta}\right] \tag{3.3}$$

where B_p is the polar value of the magnetic field, R_{NS} is the star radius, a prime denotes a derivative with respect to $\mu \equiv \cos\theta$, $0 \le p \le 1$ is the radial index, $f = f(\mu)$ is a function of μ^3, and C is a constant. The value of p settles the amount of shear of the field as well as controlling the radial decay. The footpoint of a (closed) magnetic field line will be rotated by a net angle $\Delta\phi$, the twist angle, defined as:

$$\Delta\phi = \int_{\text{field line}} \frac{B_\phi}{(1-\mu^2)B_\theta} d\mu = \left[\frac{C}{p(1+p)}\right]^{1/2} \int_0^1 \frac{f^{1/p}}{1-\mu^2} d\mu \tag{3.4}$$

---

[3] It satisfies the Grad-Shafranov equation: $(1-\mu^2)f'' + p(p+1)f + Cf^{1+2/p} = 0$.

Decreasing p, B_ϕ increases, with respect to the other components, and consequently the twist increases. In fact, the radial index is a decreasing monotonic function of $\Delta\phi$ and $B \propto r^{-(2+p)}$; the higher the twist of the field lines the more attenuated is the radial dependence of the magnetic field. When $p = 0$ the magnetic field tends to a split monopole, while when $p = 1$ we have an untwisted dipole. This model depends on the possibility of having a current in the magnetosphere, hence on a plasma that can conduct it. The required current is $\vec{j}_B = (c/4\pi)\vec{\nabla} \times \vec{B}$ and a minimum plasma density $n_e = j_B/(ec)$ is needed [51].

The presence of a magnetospheric twist influences the evolution of a magnetar. For instance, the emission and the long terms evolution before or after a series of bursts or a giant flare has frequently been explained by the gradual establishment and the successive decay of a magnetospheric twist [52]. In this scenario, in fact, the rising of a progressively growing twist makes the optical depth for resonant cyclotron scattering (RCS), i.e. the scattering at the cyclotron resonance (with $\epsilon_B = \hbar eB/(m_e c) = 11.6B_{12}$ keV the electron cyclotron energy) of thermal seed photons onto electrons in the magnetosphere, to increase and, consequently, the X-ray spectrum to gradually harden. Concurrently, the spin-down rate is enhanced because, for a fixed dipole field, a growing fraction of field lines opens out across the light cylinder, $R_{\rm lc} = cP/2\pi$ [8]. Indeed, the presence of a twist makes the magnetic field to decrease more slowly than $\sim R^{-3}$, and, as a consequence, the spin-down rate increases, since the rate of rotational energy loss is $I\Omega\dot{\Omega} \sim B(R_{\rm lc})R_{\rm lc}^2 c \propto B(R_{\rm lc})$ [50]. Moreover, the growth of the twist angle and consequently of the spin-down rate leads to an increase of the measured spin-down power and a decrease of the characteristic age, due to the fact that both quantities are related to $\dot{P}$ [8]. The twist will then relax and decay outside the star.

3.3.2 Evolution of the twist

The twist, once formed in the magnetosphere, after a certain amount of time $t_{\rm decay}$ has to decay. If it were a genuinely static twist, for which $\partial B/\partial t = 0$, the electric and magnetic field would be orthogonal. This would imply that, between the two footpoints of a magnetic field line, the voltage drop would vanish because the parallel component of the electric field would be zero, $E_\| = 0$ [8]. Hence the required current to support the non-potential field would not be present, since no force would be able to extract particles from the surface and lift them against gravity to trigger the current. Therefore, the decaying of the twist is necessary to provide that potential drop needed to lift charges from the surface and accelerate them to initiate the current [48]. The key ingredient is the self-induction of the slowly decaying current, which is able to generate and sustain the $E_\|$ field. The latter substantially measures the rate of the decay of the twist, but when it exceeds a critical value, $e^\pm$ avalanches are triggered in the magnetosphere, and the created pairs screen the electric field. The "bottleneck" for the untwisting of the magnetosphere is reached, which results in a slow decay [51]. The X-ray spectrum and the pulse profile will be modified by the persistent currents flowing outside the star, which will heat its surface. The magnetospheric twist is controlled by the value of the conduction current j with respect to j_B, in fact $\partial E_\|/\partial t = 4\pi(j_B - j)$:

- $j < j_B$: $E_\|$ grows at the expenses of the magnetic field and more charges are provided to the magnetosphere;

- $j > j_B$: this time the field decreases, hence the current is reduced.

A dynamical (quasi-) equilibrium is then reached when $j \sim j_B$, for a timescale $< t_{\rm decay}$ [8]. The value of the potential drop is kept near to the pair production threshold $e\Phi \approx 1$ GeV, and the rate of magnetic energy dissipation is $\dot{E}_{\rm mag} \approx I\Phi$, where $I \approx j_B l^2$ is the current and l is the scale-length of the twisted region [51]. Long term (months or years) variations are observed in several magnetars after a period of activity or a flare. If this was due to the decaying twist, then the decay time would be of the order of 1–10 yr. As we can see, the magnetic energy stored in the twist is $E_{\rm mag} \approx I^2 R_{NS}/c^2$, and the twist decay time is [50]:

$$t_{\rm decay} \approx \frac{E_{\rm mag}}{\dot{E}_{\rm mag}} \approx 40\Delta\phi^2 \left(\frac{L_X}{10^{35}\ \text{erg s}^{-1}}\right)^{-1} \left(\frac{B_{\rm d}}{10^{14}\ \text{G}}\right)^2 \left(\frac{R_{NS}}{10\ \text{km}}\right)^3 \text{yr}, \tag{3.5}$$

and for typical parameter values, it turns out to be $\sim$ 1yr.

The evolution of an untwisting magnetosphere, more details in [49], proceeds through the expansion of a potential region, where $\nabla \times B = 0$, which progressively confines the twist to a limited bundle of current-carrying field lines (the j-bundle) until the twist is completely erased.

3.3.3 Composition of the magnetosphere

A corona forms around magnetars, but its emission is not powered by the star rotation. In fact, all observed magnetars are slow rotators and the coronal emission can not be sustained by the rotational energy alone [51]. Instead, it is the presence and the evolution (decay) of the magnetic twist which influences the composition of the magnetosphere. The dissipation of the energy stored in the non-potential (toroidal) magnetic field is able to explain the observed activity of the corona.; closed magnetic lines, extending up to $R_{\rm max} \sim 10R_{NS}$, carry the stored energy [51]. The order of magnitude of the permanence time of the particles in the corona is much lower than the evolutionary timescale of the magnetic field, hence the latter can be thought of as fixed. Moreover, particles move strictly along the magnetic field lines forming a current $j \sim j_B$.

The simplest model [50], which is also the one that will be used in this work, neglects pair production. In this scenario, we only have two currents, composed of electrons and ions, ensuring charge neutrality, which move in opposite directions. The definition of the magnetic topology and of the particle velocity automatically settles the density of particles in the magnetosphere. The latter can be obtained from the condition $j = j_B$, needed to ensure a dynamical equilibrium in the globally twisted force-free magnetic field, that gives [53]:

$$n_e(\vec{r}, \beta) = \frac{p+1}{4\pi e} \left(\frac{B_\phi}{B_\theta}\right) \frac{B}{r|\langle\beta\rangle|} \tag{3.6}$$

where $|\langle\beta\rangle|$ is the average charge velocity in units of c. The co-rotation charge density of the space charge-limited flow of ions and electrons from the stellar surface is normally given by the Goldreich-Julian density, n_{GJ}. In this case, instead, n_e is much larger than n_{GJ} because of the closed loops present in twisted fields. The current is composed of positive charges, with density n_+ and velocity v_+, and by negative charges, with density n_- and velocity v_- flowing in the opposite direction; it is given by $j = j_B = e(v_+n_+ - v_-n_-)$ and we have $v_+v_- < 0$ [8]. The general assumption is that electrons move from north to south and the other way round for ions, hence breaking the symmetry between the two hemispheres. In such strong magnetic fields, e^- flow freely along closed field lines while being confined in a set of cylindrical Landau levels in the plane perpendicular to B, which makes the electron distribution to be widely anisotropic. In most models, including the one used in this thesis, the "unidirectional flow" is used, where only the currents of electrons are considered. As a matter of fact, ions add only little contribution to the spectra of the star, for example in the scattering with photons they can at most generate a narrow absorption feature at the cyclotron energy [23]. When ions, and the consequent effects, are taken into account we talk about "bidirectional flow" models. A discriminating factor between the various models is the choice of the velocity distribution of the scattering charges [54]. The latter, in fact, is assumed to be spatially independent, which makes the charge velocity a free parameter of the model. However, the observed X-ray spectra need a mildly relativistic charge velocity, $\gamma \simeq 1$, to be reproduced.

A realistic physical model would take into account also the production of pairs in the magnetosphere, as in [51]. In this scenario, the electric field $E_{\parallel}$ is created by the self-induction of the field, and the voltage drop between the two footpoints of a magnetic line is able to transfer the magnetic energy, released by the untwisting of the magnetic field, to the charged particles, accelerating them. When the magnetic field B exceeds the critical quantum value B_Q, one-photon pair production becomes possible in two steps, because it would need photons with energy higher than the threshold value ~ 1 MeV. At first, electrons moving along a magnetic field line and accelerated to $\gamma = \gamma_{\text{res}} \sim (m_e c^2/\epsilon)(B/B_Q) \sim 1000$ by the electric field, where γ_{res} is the electron Lorentz factor at the resonance, undergo resonant scattering with a thermal X-ray photon with energy $\epsilon \sim 1$ keV. Also the latter process may be considered as two-step: (i) the electron is excited to the first Landau level (corresponding to the electron cyclotron energy ϵ_B), then (ii) it rapidly de-excites emitting a photon. The emitted photon has a considerable energy $\epsilon' \sim \gamma_{\text{res}}^2 \epsilon/(1 + \gamma_{\text{res}}\epsilon/m_e c^2)$, hence quite instantaneously it converts to a $e^{\pm}$ pair via single photon pair production [39]. This process requires a much smaller electron Lorentz factor with respect to the one occurring in radio pulsars, where electrons need to be accelerated up to $\gamma_e \sim 10^7$ to produce gamma rays which convert to $e^{\pm}$ pairs [51]. These pairs created can also give rise to returning current effects.

3.3.4 Resonant Compton Scattering

Now we want to see a little more in detail the processes that arise in the magnetosphere due to the presence of the particles lifted from the surface. The first-order process in which a photon excites a particle from a lower to a higher Landau state is cyclotron absorption. However, the cyclotron decay rate is much higher than the collisional one [55], hence radiative transitions overcome collisions [39]. As a consequence, when an electron undergoes cyclotron absorption, since the decay rate is rather high and makes all particles occupy the ground state, it will de-excite emitting another photon, instead of collisionally de-exciting. In the end, the resulting process is a photon scattering in place of true absorption. Thanks to this, an X-ray photon can be converted into a γ-ray one. As we saw in the previous section, in the magnetar case the presence of currents $j_B = (c/4\pi)\nabla \times B$ extending in the magnetosphere requires a minimum plasma density $n_e = j_B/ec$. Even this minimum density has strong implications in shaping the emergent spectrum of stellar radiation. The thermal photons emitted from the cooling surface constitute only a little radiative output. If the plasma is sufficiently hot, the charges flowing along the closed field lines of the twisted magnetosphere can Compton upscatter the thermal surface X-rays. Electron scattering is largely influenced by the presence of a strong magnetic field, in particular, the cross section has a more pronounced dependence on the photon energy and the incident angle. The main effect is the appearance of the cyclotron resonance, with ϵ_B the electron cyclotron energy. If photons have energies far greater than the resonance one, $\epsilon \gg \epsilon_B$, then $\sigma = \sigma_T$; instead, when $\epsilon \ll \epsilon_B$ the magnetized plasma becomes quite optically thin to photon frequencies below the cyclotron one [39]. The surface emits a thermal photon with energy lower than the electron cyclotron energy; then it passes through the magnetosphere encountering the electron cyclotron resonance, where multiple scatterings may take place and will spread photon frequency. Backscattered photons will move to the surface with energy lower than the resonant one and they undergo subsequent resonant scatterings. The magnetospheric current-carrying charges provide a significant optical depth to resonant cyclotron scattering. Following [50], if Ze, M and $\omega_c = ZeB/Mc$ are the charge, the mass, and the resonance frequency of the particles respectively; ω is the incoming photon frequency while θ_k is its angle with respect to $\vec{B}$, then the radius at which the resonant surface sits is given by:

$$R_{\text{res}} = \left(\frac{ZeB_\theta}{Mc\omega}\right)^{1/3} f(\theta), \tag{3.7}$$

where $f(\theta)$ is the angular function. As it can be seen in the latter formula, resonance of photons with frequency ω will be located at different radii, depending on the particles they are scattering with, namely electrons or ions; from the equilibrium condition, instead, it follows that the magnetosphere hosts more than one scattering corona: the electron one at $R \sim 50$–100 km from the surface and the ion one closer to the star surface at $R \sim 10$–20 km. When the latter is composed of ions of different charge/mass ratios Z/M scattering is more efficient. Indeed, in this way, multiple scattering layers will form according to the charge/mass ratio; heavier ions will resonantly scatter surface photons closer to the star, conversely for lighter ones. As a consequence, both inward, backscattered, and outward photons can resonantly scatter. Now if we define ϵ^Z the current fraction carried by particles and $v^Z \leq c$ their drift velocity, we can write the optical depth for resonant scattering as:

$$\tau_{\text{res}} = \frac{\pi\epsilon^Z}{4}(1+\cos^2\theta_k)\left(\frac{c}{v^Z}\right)\left(\frac{p+1}{p+2}\right)\left[\frac{F(\theta)}{F(\pi/2)}\right]^{1/p}\left(\frac{B_\phi}{B_\theta}\right)_{\theta=\pi/2}. \tag{3.8}$$

Here $[F(\theta)]^{1/p} \simeq \sin^2\theta$ for a magnetospheric twist $\Delta\phi \lesssim 1$ radian. Therefore the optical depth is highly anisotropic: surface radiation will be strongly scattered at the cyclotron resonance near the equatorial plane, while it will emerge almost unscattered near the magnetic axes (the poles), where the optical depth approaches zero and the equilibrium current density is reduced as a result of the large extent of the field lines.

The magnetospheric reprocessing of the surface field gives rise to a high energy non-thermal, powerlaw-like tail. This may explain the spectrum observed both in the 0.1–10 keV energy range and in the hard X-ray one [8]. The hardness of this tail seems to be correlated with the magnetospheric shear: the stronger the overall twist imparted to the magnetic dipolar field, the harder the power law tail. Also, the tendency of increasing spectral hardness with the overall bursting activity may be explained by the RCS model.

3.4 Surface emission models

As we saw a simple blackbody is not suitable to describe the thermal radiation emitted from the magnetar. Beyond the reasons mentioned above, more physically motivated models of the surface radiation should be taken into account, to have an improved characterization of the spectral and polarization properties of magnetar persistent emission within the RCS scenario. Although the features of the outermost layers of a highly magnetized neutron star are still debated, the thermal component itself may either arise directly from the surface in a condensed state or be reprocessed by some sort of (non passive) magnetized atmosphere. Taverna et al. [3] computed the spectra, through Monte Carlo simulations, that may originate from a condensed surface (in both the free/fixed ion limits) and from a magnetized hydrogen atmosphere. In their analysis the star is assumed to be an aligned rotator ($\xi = 0$) with a globally twisted dipole field with $B_p = 5 \times 10^{14}$ G; a unidirectional flow is also assumed, with β the speed of electrons along the (closed) field lines superimposed on a 1D Maxwellian distribution. As it can be seen in figures 3.2, 3.3, 3.4, 3.5, according to their simulations, the results of spectral observations alone, including or not magnetospheric RCS, did not differ much from a 100% polarized blackbody plus a powerlaw distribution in the former case and a 100% polarized blackbody in the latter. The underlying emission model is far more relevant when looking at polarimetric measures, as we will see in section 3.6.

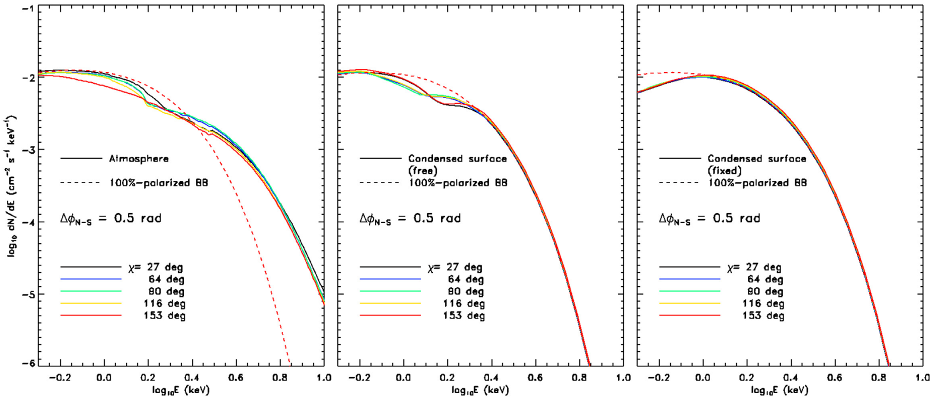

Figure 3.2: The number flux as a function of the photon energy is depicted for a 100% polarized blackbody spectrum, dashed line, and an atmosphere (left), condensed surface with free (middle)/fixed (right) ions as seen by an observer at infinity. The star is an aligned rotator ($\xi = 0$) and is observed at different inclinations χ. The magnetic field is a globally twisted dipole with $\Delta\phi = 0.5$ and $B_p = 5 \times 10^{14}$ G. Image taken from [3]

3.4.1 Atmosphere

The generally adopted scenario consists of a gaseous atmosphere covering the neutron star, with a typical density of $\sim 10^{-3}$–10^{-4} g cm^{-3} [39] and a scale height $H \sim kT/m_p g \simeq 0.1$–$10$ cm [3], with T the surface temperature, m_p the proton mass, and g the surface gravity. Of course the radiative opacities, the chemical composition and the equation of state of the atmosphere will directly impact on the thermal emission features [39]. The returning currents generated by the twisted magnetosphere also play a fundamental role in the heating of the external layers of a magnetar [51]. While different magnetization and chemical compositions (H, He and heavy elements) have been accounted for by many authors seeking a model atmosphere, e.g. [56], a full analysis of the effects of backflowing charges on the atmosphere has not been carried out yet. Finally, the thin atmospheric layer is anisotropic and birefringent due to the presence of a huge magnetic field [39].

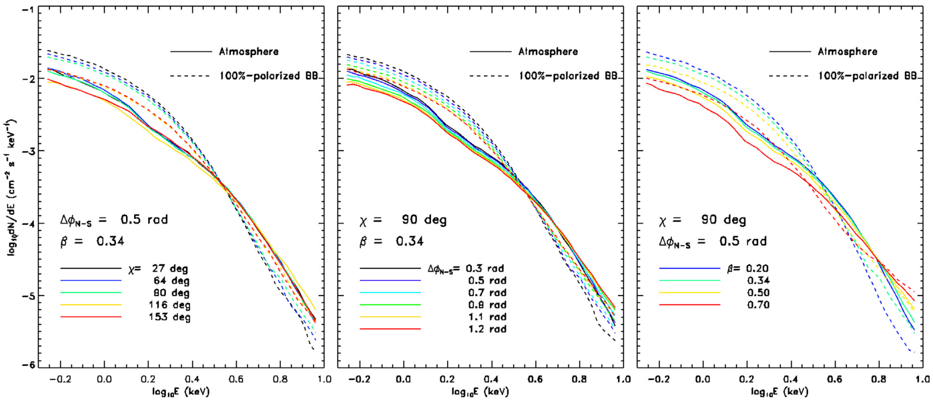

Figure 3.3: Simulated number flux as a function of the photon energy from a 100% polarized blackbody seed photons, dashed lines, and a magnetized, partially ionized H atmosphere, solid lines, taking into account also the effects of RCS. An aligned rotator ($\xi = 0$) with $B_p = 5 \times 10^{14}$ G is considered and in the left, middle and right panel the inclination (χ), the twist angle ($\Delta\phi$) and the electron velocity (β), respectively, are varying. Image taken from [3]

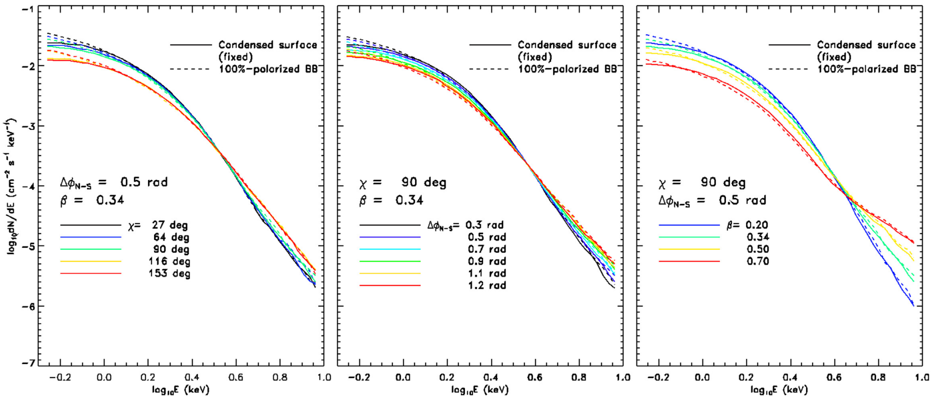

Figure 3.4: Same as in 3.3 but considering an emission in the case of a condensed surface in the fixed-ion limit. Image taken from [3]

3.4.2 Condensed surface

The properties of matter substantially change in fields $B \gtrsim 10^{12}$–10^{13} G. Highly elongated atoms can form molecular chains and the dipole-dipole attraction of these chains may lead to a phase transition which transforms the star surface in a condensed state, either liquid or solid [57]. Such a phase transition occurs at a critical temperature $T_{\rm crit}$, which in turn depends on the surface strength of the magnetic field and the chemical composition [58]. The critical temperature, for a H condensed surface, increases with increasing B [59]. The atmosphere covering the neutron star surface may arise from a first-order transition between condensed matter and non-degenerate plasma. If it is absent (then the star will be called naked) or optically thin, the radiation is emitted by the solid or liquid surface without reprocessing in a gaseous atmosphere [56]. It will be polarized and its polarization properties will depend on the dielectric tensor of the medium, affected by the presence of bound species [39], and in an equally nontrivial way on the frequency and angles. Also the characteristic of the emerging spectrum will be influenced by the emission features of the condensed surface, like for example its reflection properties. It is commonly used the approximation of a fully ionized electron-ion plasma with either non-moving ions (also called fixed-ion limit) or of finite-mass ions freely responsive to the electromagnetic forces (the free-ion limit). As usual, *in medio stat virtus*: Coulomb forces between ions tone down their response, but not to the point where they can stall ions in their equilibrium positions. Moreover, incomplete ionization may be present with bound electron shells embedded in the plasma, which may be anticipated in a shallow layer beneath the surface [3].

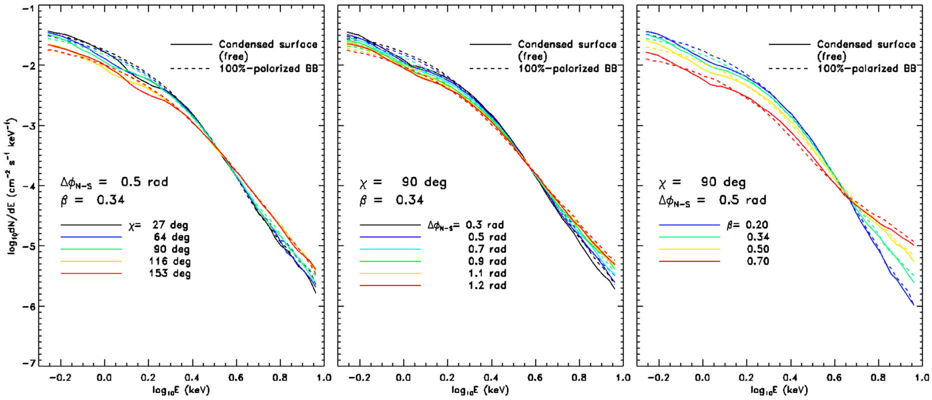

Figure 3.5: Same as in 3.3 but considering an emission in the case of a condensed surface in the free-ion limit. Image taken from [3]

3.5 Spectral observations

In this section, we want to analyze the magnetar emission, the information that we can infer from their spectral observations and the capability of the model described in the previous section in explaining the observed data.

Up to now 30 magnetars are known, among which 16 are classified as SGRs (12 confirmed and 4 candidates) and 14 as AXPs (12 confirmed and 2 candidates) [60].[4]

---

[4] The complete and updated list of magnetars can be found at `http://www.physics.mcgill.ca/~pulsar/magnetar/main.html`

Among them some are classified as transient and, as we saw, their quiescent emission might be too low for the sensitivity of our instruments. This makes us wonder if there might be a large number of undiscovered magnetars which have a luminosity too low to be detected; if this was the case then a higher number of sources classifiable as magnetars and hence a higher magnetar birthrate would have to be accounted for.

Measuring period and period derivative of magnetars we can infer information about the rotational energy loss, thought to be regulated principally by the external magnetic field dipolar component. Magnetars X-ray luminosities varies from the huge $L_X \approx 10^{44}$–10^{47} $\mathrm{erg\,s^{-1}}$ of the rare giant flares, with duration of $\Delta t \simeq 100$–1000 s, passing from $L_X \approx 10^{36}$–10^{43} $\mathrm{erg\,s^{-1}}$ of the short bursts, with $\Delta t \simeq 0.01$–50 s, up to the persistent one in the $\simeq 0.5$–200 keV band $L_X \simeq 10^{31}$–10^{36} $\mathrm{erg\,s^{-1}}$. Apart from the dramatic variation in the flux of transient magnetars, also all the others magnetars has shown long terms variability in their emission, which can modify their spectra, pulse profile and spin-down rate. The timescale of this variation can either be long, with gradual changes in the flux, or short, like glitches, bursts or sudden outbursts. The latter might be due to a sudden reconfiguration of the magnetosphere, when unstable conditions are reached. This phenomenon involves a large range of energies, the most dramatic one being the giant flares, and may cause starquakes and/or instabilities in the outer magnetosphere (presumably involving magnetic reconnection) [8]. The soft X-ray emission long term decay can be explained by the heating and consequent cooling of the magnetar crust. The former might appear consequently to crustal plastic deformations which provoke changes in the magnetic current configurations. In a twisted magnetosphere, as stated in the previous section, both impact of the current-carrying charges on the stellar surface, and the resonant Compton scattering of the magnetospheric currents with the surface flux result in an X-ray emission. A source can undergo both kind of variability, one does not exclude the other.

3.5.1 Persistent emission

Soft X-ray emission

The soft X-ray (0.1–10 keV) energy band is the main observation range of X-ray satellites such as XMM-Newton, Chandra and Swift. After a large amount of observations, magnetars persistent spectra have an X-ray luminosity of 10^{35}–10^{36} $\mathrm{erg\,s^{-1}}$, and are typically found to be fitted in this range by a thermal component, given by a blackbody with $kT \sim 0.5$–1 keV, and a non-thermal one, a high energy, steep powerlaw tail with photon index $\Gamma \simeq 2$–4 [14]. The more plausible mechanism that can give rise to the observed magnetars spectral shape is the resonant upscattering of surface thermal photons in the corona. The mildly relativistic magnetospheric charges would distort the thermal radiation coming from the surface through resonant cyclotron scattering. Few sources are well-fitted only by two distinct thermal components [61], for example transient sources often show a purely thermal spectrum. This suggests us that the origin of the soft X-ray emission is preponderantly thermal, still the observed spectrum is more complex than a blackbody at a single temperature.

Interestingly, a relation between temperature and magnetic field can be inferred comparing the average temperature [62], derived from thermal luminosity, of magnetars with those of other classes of isolated neutron stars. Magnetars, in fact, are systematically more luminous than rotation-powered neutron stars of comparable characteristic age [63]. The data seem to confirm the correlation between spin-down rate and the hardness of the soft X-ray powerlaw photon index Γ [64] [65], but only for rotational frequency derivatives $\dot{\nu} \gtrsim 10^{-14}$ s^{-2}, and with some exceptions – like transient magnetars in outbursts and the recently discovered low-B magnetars. The RCS model corroborates the aforementioned relation: an increasingly twist angle of the magnetic field will generate a larger spin-down rate and will also inject a higher number of particles in the magnetosphere, which will lead to a harder spectral tail [8].

Resonant scattering, in principle, might result in the presence of spectral lines, that if detected could bring to a direct measurement of the neutron star magnetic field intensity. For magnetic fields of the order of $\sim 10^{14}$–10^{15} G, the electron cyclotron lines would lie in the unobserved range above ~ 1 MeV, instead, proton ones could be present in the X-ray range, at the proton cyclotron resonance $E_{c,p} \simeq 0.63 z_G (B/10^{14}\text{G})$ keV, where z_G is the gravitational redshift [14]. The persistent emission of magnetars, up to now, has shown presence of an absorption line in SGR $0418 + 5729$ [66]. Pulse profiles of magnetars are variegated. Few magnetars are found to have an (almost symmetric) double-peaked light curve with a 10–20% pulsed fraction [67], among which 4U 0142+0162 [68], the source on which we are focused in this work; the vast majority, conversely, exhibit a single peaked pulsed component with pulsed fraction that can exceed 50–60%.

Hard X-ray emission

The vast majority of magnetars exhibit a higher bolometric luminosity in the hard X-ray range rather than in the soft one, e.g. [69] [70]. In fact, a large fraction of the total persistent flux is emitted at energies well above ~ 20 keV and it is observed to peak above 100 keV, extending to ~ 150 keV, with a luminosity $\sim 10^{36}$ erg s^{-1}. This emission has a non-thermal (powerlaw) character. Moreover, the hard tail of the soft emission is often seen to have a different powerlaw slope with respect to the hard one [71]. The spectral location of this turning point is being searched and it is expected to correlate with B_d [72]. This hints at the emission mechanism in the two energy band to be distinct, or at different properties of the charges in the hard X-ray range [8]. No confirmed emission above a few hundred keV has been detected by high energy observatories, like Comptel and Fermi LAT; this is a symptom of a possible spectral break with the cutoff between 200 keV and 1 MeV [73].

The hard energy emission mechanism has not been unveiled yet and several models have been proposed, all of them requiring continuous particle acceleration during the persistent state. The keystone would be the solution of the force-free equation $\nabla \times B = \alpha(x) B$, but unfortunately no techniques have been developed up to now. An explanation of the spectral break may come from the consideration of the effects of electron recoil and multiple scatterings from high energy photons, which require the use of the full quantum electrodynamics (QED) cross section. It is not possible to estimate or predict the energy at which such a break may occur, because it depends on the features of the magnetic field topology and of the distribution of currents, as well as on the effect of repeated scatterings. If we took ultra-relativistic magnetospheric electrons, the emerging spectral tail would be flat and unbroken, even up to energies > 1000 keV, regardless of magnetic topology and cross section details [8]. Studying at the same time both hard and soft X-ray spectra allows one to analyze possible links between the variability in the two bands, while high resolution pulsed phase spectroscopy may unfold the particulars of the slope turn-over (when present) in the soft-to-hard emission.

3.5.2 Bursting emission

SGRs sources discovery is often due to the detection of repeated soft gamma-ray bursts [74], hence their name, which is one of their distinctive features. AXPs were also seen to emit SGR-like bursts [75]. The energy range spanned by the bursting emission is really wide, from few keV in the soft X-rays to hundreds of keV in the hard X-rays/soft γ-rays. The time between two events can span just few hours to even years. In the former case we talk about phases of high burst activity, which can culminate in burst storms or even giant flares; the latter, conversely, are periods of quiescence, when only sporadic and highly occasional bursts happen, or maybe bursts occur more frequently but below the detection threshold of present-day telescopes. The characteristics of the overall emission might change following the periods of activity, for example the spin-down rate was observed to increase, as well as the spectral hardening [76]. On the other hand, the dipolar magnetic field strength of the source seems to be unrelated to short/intermediate bursting activity; in fact, stars with field strengths lower than the critical quantum limit $B \lesssim B_Q$ exhibit bursts too[5] [77][78]. Giant flares, instead, were observed from sources possessing a dipole field among the highest – a few times 10^{14} G up to $\sim 10^{15}$ G.

Bursts are usually divided into three categories depending on their duration and energy release. The first type are the most common short bursts, with emitted energies in the range 10^{36}–10^{41} erg [79][80]. The lowest luminosity observed corresponds to the sensitivity of the current generation of instruments. The shape of the lightcurves are incredibly varied and a simple phenomenological model that could explain the various conformation is still missing. The extended duration of the tail can make its releasing of energy higher than that of the original spike [81]. The time interval between two bursts spans a wide range, from ~ 1 s to more than 1000 s [82], climaxing in $\sim$ years of quiescence, and is not affected by the burst intensity [83]. Usually no emission from short bursts is detected above 150–200 keV.

The second type are the intermediate flares, with energies in the range $\sim 10^{41}$–10^{43} erg. Usually they are composed by a primary burst which resembles the short bursts, but brighter and longer (it has a duration of ~ 0.5 s up to a few seconds), and sometimes they can have short precursors[84]. In some cases the primary burst decays and then has an abrupt end [85], in other cases, instead, it is followed by a long decaying tail which might last several hundreds seconds, but contains however only $\lesssim 2\%$ of the primary peak energy [84]. If a tail is present, it is pulsed at the rotational period of the star, has different spectra with respect to the primary burst, and some short bursts might appear[84].

The last type are the hugely energetic, and extremely rare, giant flares. The total energy released in these extraordinarily powerful events is in the range 10^{44}–10^{47} erg. Only three magnetars (SGR 0526-66 [86], SGR 1900+14[87], and SGR 1806-20 [88]) were seen to emit a giant flare and just one each. The features of this emission are highly similar, apart from the different amount of energy released. A very bright initial peak is detected with a subsequent decaying tail, which lasts up to several hundreds seconds and is strongly pulsed at the rotational frequency of the star[89]; in addition, two of the three giant flares exhibited a precursor. The initial peak lasts ~ 0.1–1 s, is very hard and can have a rise time as short as ~ 1 ms. Its reliable spectral modelling is tremendously complicated by the dead time and pile up effects in space telescopes,

---

[5] The spin-down estimate of the dipole field strength is only a lower limit, therefore a higher order poloidal or toroidal component can not be excluded.

which arise as a result of the extremely high luminosity reached, 10^{47} erg s^{-1} [89]. The resulting spectra, however, are very hard, with emission being detected up to 2 MeV. The tails of the three giant flares were seen to release a comparable amount of energy, $\sim 10^{44}$ erg.

3.5.3 Emission at other wavelengths

The fact that magnetars do not emit in the radio band was thought to be one of their defining properties until a radio signal was observed in XTE J1810-197 [90]. Its emission is thought to have started about a year after the beginning of an X-ray outburst and lasted a few years. The radio flux and the pulse shape were markedly variable. The first, and up to now the only one, magnetar to be discovered thanks to radio observations, is PSR 1622-4950 [91], which is probably a transient magnetar that experienced an outburst in 2007. By comparing radio-loud magnetars with radio pulsars, we see that the radio emission features of these two kinds of sources are very different [92]. An interesting property that was observed in radio-loud magnetars, at variance from what is observed in radio-silent ones, is that during quiescence these sources display a luminosity in the X-ray energy band lower than the rotational energy loss rate $L_X < \dot{E}$, as it happens also in other classes of neutron stars [93]. However, the contrary is not true, not all sources with $L_X < \dot{E}$ show a radio emission. Moreover, radio afterglows were detected after both the SGR 1900+14 and SGR 1806-20 giant flares [94] [95]. Their energies are much less than that emitted in the γ-rays, at variance from GRBs; they are observed to be linearly polarized and to expand over time. It was hypothesized that Fast Radio Burst might originate from magnetars, either from the interaction of the relativistic ejecta (expelled by the initial spike of the giant flare) and the surrounding wind nebula [96], or from a magnetar/Be binary [97].

AXPs and SGRs have been discovered to emit also in the optical and/or near-infrared (NIR) bands [98]. The optical/NIR counterparts are faint and their flux is only a small fraction of the bolometric flux; still their detection can place important constraints on models. Two mechanism may explain this emission: it can have a magnetospheric origin [99], or it may originate in an extended disk. The latter seems to be the case for the source analyzed in this work and, if confirmed, it would be the first detection of a supernova fallback in any context [100].

3.6 Polarization

3.6.1 Stokes parameters

By definition a monochromatic plane wave is linearly polarized – its electric field oscillates along a specific direction. If we consider the superposition of two waves at a specific point in space (we can take $\vec{r} = 0$ without loss of generality), taking a reference frame with $\vec{k} \parallel \vec{z}$ and with $\vec{x}$, $\vec{y}$ the unit vectors of the x and y axes, the total electric field will be given by:

$$\vec{E} = (\vec{x}E_1 + \vec{y}E_2)e^{-i\omega t} = \vec{E}_0 e^{-i\omega t} \tag{3.9}$$

where the amplitudes $E_{1,2}$ are in general complex: $E_{1,2} = \xi_{1,2}e^{i\phi_{1,2}}$. So we can write the total electric field as

$$\vec{E} = \vec{x}\xi_1 e^{i(\phi_1 - \omega t)} + \vec{y}\xi_2 e^{i(\phi_2 - \omega t)} \tag{3.10}$$

Hence, the physical field along the x and y directions will be given by the real part of the projection of this complex-valued vector along those directions:

$$E_x = \mathrm{Re}\left\{\xi_1 e^{i(\phi_1-\omega t)}\right\} = \xi_1\cos(\phi_1-\omega t) = \xi_1\cos\omega t\cos\phi_1 + \xi_1\sin\omega t\sin\phi_1, \quad (3.11)$$

$$E_y = \mathrm{Re}\left\{\xi_2 e^{i(\phi_2-\omega t)}\right\} = \xi_2\cos(\phi_2-\omega t) = \xi_2\cos\omega t\cos\phi_2 + \xi_2\sin\omega t\sin\phi_2. \quad (3.12)$$

This coincides with the parametric equation of an ellipse obtained from the rotation by an angle χ of the principal axes:

$$x = A\cos\beta\cos\chi\cos\omega t + A\sin\beta\sin\chi\sin\omega t, \quad (3.13)$$

$$y = A\cos\beta\sin\chi\cos\omega t - A\sin\beta\cos\chi\sin\omega t, \quad (3.14)$$

with $A \in \mathbb{R}^+$ and $\beta \in [-\pi/2, \pi/2]$; hence, we identify:

$$\xi_1\cos\phi_1 = A\cos\beta\cos\chi \quad (3.15)$$

$$\xi_1\sin\phi_1 = A\sin\beta\sin\chi \quad (3.16)$$

$$\xi_2\cos\phi_2 = A\cos\beta\sin\chi \quad (3.17)$$

$$\xi_2\sin\phi_2 = -A\sin\beta\cos\chi. \quad (3.18)$$

This means that the tip of the electric field vector rotates along an ellipse which is tilted with respect to the x, y axes by an angle χ. From these four equations, we can define the Stokes parameters I, Q, U, V:

$$I \equiv A^2 = \xi_1^2 + \xi_2^2 = \xi_0^2 \quad (3.19)$$

$$Q \equiv A^2\cos 2\beta\cos 2\chi = \xi_1^2 - \xi_2^2 \quad (3.20)$$

$$U \equiv A^2\sin 2\chi\cos 2\beta = 2\xi_1\xi_2\cos(\phi_1-\phi_2) \quad (3.21)$$

$$V \equiv A^2\sin 2\beta = 2\xi_1\xi_2\sin(\phi_1-\phi_2). \quad (3.22)$$

They completely describe the state of an elliptically polarized monochromatic wave. Reversing these definitions we can find the parameters of the ellipse:

$$A = \sqrt{I}, \quad (3.23)$$

$$\sin 2\beta = \frac{V}{I}, \quad (3.24)$$

$$\tan 2\chi = \frac{U}{Q}. \quad (3.25)$$

I is connected to the intensity. In fact, from equation (3.19) we know that $\xi_0 = A = \sqrt{I}$ and the energy flux is given by:

$$S = \frac{c}{4\pi}\xi_0^2 = \frac{c}{4\pi}I; \quad (3.26)$$

so the parameter I is directly proportional to the energy flux S. The semi-major and semi-minor axes of the polarization ellipse are $2A\cos 2\beta$ and $2A\sin\beta$, respectively, therefore $\tan\beta$, their ratio, measures the eccentricity of the ellipse and can be recovered from V/I, as one can see from equation (3.24). Instead, the ratio U/Q in equation (3.25) describes the orientation of the ellipse with respect to the x and y axes. When $V > 0$ the polarization is left-handed, while when $V < 0$ the polarization is right-handed; if $V = 0$

the wave is linearly polarized (because the ellipse collapses). Instead, if $U = Q = 0$ and $V \neq 0$ we have circular polarization.

The four Stokes parameters are not independent; in fact, we need only three parameters to describe the ellipse. Indeed, they are connected by the relation $I^2 = Q^2 + U^2 + V^2$, but this is only valid for totally polarized, monochromatic waves. In the general case, for partially polarized radiation, we have instead $I^2 \geq Q^2 + U^2 + V^2$. Finally, for completely unpolarized light we have $Q = U = V = 0$. The Stokes parameters are additive: the superposition of waves with different Stokes parameters can be described by the sum of the Stokes parameters of the single waves. We can write the Stokes parameters as a vector:

$$\vec{S} = \begin{bmatrix} I \\ Q \\ U \\ V \end{bmatrix}. \tag{3.27}$$

Since we can, in general, decompose partially polarized radiation into a completely unpolarized part and a completely polarized part, the following can be written:

$$\vec{S} = \underbrace{\begin{bmatrix} I - \sqrt{Q^2 + U^2 + V^2} \\ 0 \\ 0 \\ 0 \end{bmatrix}}_{\text{unpolarized}} + \underbrace{\begin{bmatrix} \sqrt{Q^2 + U^2 + V^2} \\ Q \\ U \\ V \end{bmatrix}}_{\text{polarized}}. \tag{3.28}$$

This allows us to define the polarization degree, namely the fraction of the radiation which is polarized, as:

$$\Pi = \frac{I_{\text{polarized}}}{I} = \frac{\sqrt{Q^2 + U^2 + V^2}}{I}. \tag{3.29}$$

Since in our work we are dealing with extremely huge magnetic fields, we expect the circular polarization to be negligible; moreover, given that current X-ray polarimeters, based on the photoelectric effect or Compton scattering, can not measure circular polarization [101], we can take $V = 0$, which means that we will consider linear polarization. We can then analogously define the linear Polarization Degree (PD) as:

$$\Pi_L = \frac{\sqrt{Q^2 + U^2}}{I}, \tag{3.30}$$

and, in the rest of our work, when we will talk about PD, for the aforementioned reasons, we will be referring to the linear polarization degree. As a consequence, from equation (3.25), we can also define the Polarization Angle (PA) as:

$$\chi_{\text{pol}} = \frac{1}{2} \arctan\left(\frac{U}{Q}\right). \tag{3.31}$$

3.6.2 Polarization in magnetars

Radiation coming from the (cooling) magnetar surface is expected to be strongly polarized due to the presence of the extremely huge magnetic field of magnetars [102]. In fact, photons with energies $\hbar\omega$ below the electron rest-frame cyclotron energy, $\epsilon_B = \hbar\omega_B$ (which implies $B \gtrsim 10^{11}$ G at X-ray energies) are expected to be elliptically polarized

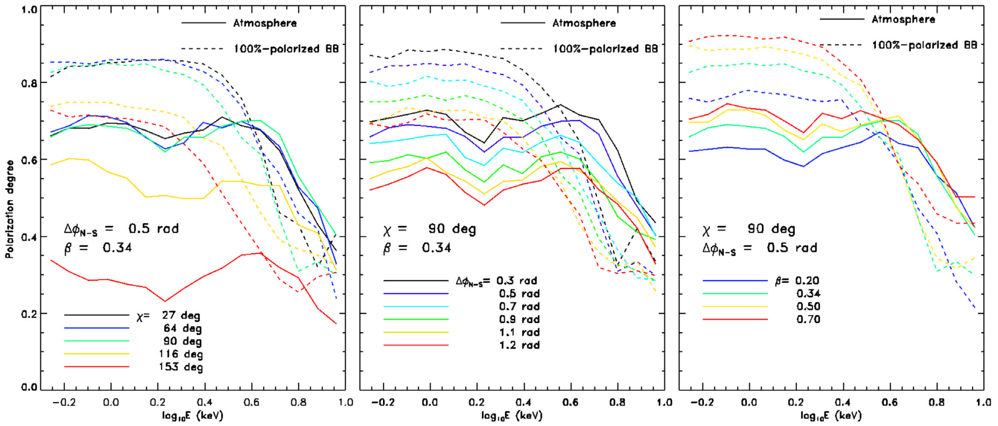

Figure 3.6: Simulated observation of the linear polarization degree as a function of the photon energy from a 100% polarized blackbody seed photons (dashed lines), and a magnetized, partially ionized H atmosphere (solid lines), taking into account also the effects of RCS. An aligned rotator ($\xi = 0$) with $B_p = 5 \times 10^{14}$ G is considered and in the left, middle and right panel the inclination (χ), the twist angle ($\Delta\phi$) and the electron velocity (β) are varying. Image taken from [3]

in two normal modes [103]: the ordinary mode (O-mode) and the extraordinary mode (X-mode). In the former case the electric field of the photon oscillates in the $\hat{k}$–$\vec{B}$ plane, where $\hat{k}$ is the unit vector along the photon direction and $\vec{B}$ is the local magnetic field, instead in the latter case the electric field oscillates perpendicularly to both $\hat{k}$ and $\vec{B}$ [39]. However, the degree of circular polarization reaches at most a few percent at X-ray energies [102], hence magnetar radiation can be assumed to be linearly polarized in these two modes. At the magnetar surface it is typically $\hbar\omega \ll \hbar\omega_B$, and, in the hypothesis that the photon energy is far enough away from the ion cyclotron energy, the seed thermal radiation is likely to be polarized for the most part in the X-mode [39]. In fact, the two modes have different absorption and scattering coefficients [56], and the opacity for the X-mode photons κ_X is much smaller than the one for the O-mode ones κ_O, $\kappa_X \sim \kappa_O(\omega/\omega_B)^2$ [39]. This means that the X-mode photosphere is located inside the O-mode one, so that X-mode photons are emitted from deeper and hotter regions with respect to the O-mode ones, thus dominating the surface thermal emission. The thermal emission from the surface regions heated by the returning currents, instead, should preferentially occur in the O-mode [51]. The presence of a strong magnetic field gives also rise to QED effects, such as vacuum polarization, that significantly influence the observed polarization state of a photon.

Section 3.5 showed that spectral observations in the 0.5–10 keV range could be explained by the twisted magnetosphere model. However, spectroscopy alone cannot provide complete information on the physical properties of the magnetosphere, due to the inherent degeneracy in the RCS model parameters [8]. In fact, as we saw in section 3.4, it is rather insensitive to both the source geometry (even if in principle it should depend on the angles ξ and χ [53]) and to the parameters that govern the magnetospheric scattering, i.e. the twist angle $\Delta\phi$ and the charges velocity β. Instead, the linear polarization fraction Π_L or PD, and PA $\chi_{\rm pol}$, measured through X-ray polarization observations, are very sensitive to all the aforementioned parameters (ξ, χ, $\Delta\phi$, β) [7]. In fact, Taverna et al. [3] simulated the persistent emission of a magnetar, and its successive reprocessing in the magnetosphere, to study how the polarization features

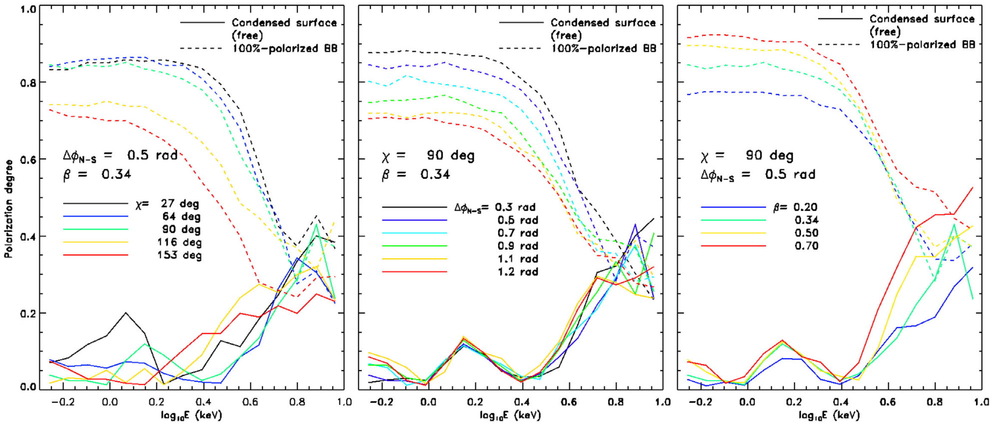

Figure 3.7: Same as in figure 3.6 but for a condensed surface in the free-ion limit. Image taken from [3]

change varying both the geometric and the magnetospheric parameters, an example can be seen in figure 3.6 and 3.7. Moreover, the latter figures also show that the underlying surface emission model (see section 3.4) has a great impact on polarization observables, as reported in those figures for PD. Polarimetric measurements in the X-rays may also provide an independent estimate of the magnetic field strength and topology [104], and can discriminate between cases in which QED effects are present or not and thus may provide an indirect evidence for ultra-strong magnetic fields [7].

Vacuum polarization

The extremely huge magnetic field of magnetars makes the vacuum around the star to behave like a birefringent medium through vacuum polarization [39]. In fact, photons propagating in the two normal modes through this vacuum can convert into virtual $e^{\pm}$ pairs, as predicted by QED; the strong magnetic field then polarizes the pairs [39], therefore the vacuum dielectric and magnetic permeability tensors (which would coincide with the unit tensor otherwise) change according to:

$$\epsilon = (1+a)\mathbb{1} + q\hat{B}\hat{B}, \tag{3.32}$$

$$\vec{\mu} = (1+a)\mathbb{1} + m\hat{B}\hat{B}, \tag{3.33}$$

where $\vec{\mu}$ is the inverse of the magnetic permeability tensor, a, q and m are functions of the magnetic field intensity, and $\hat{B}$ is the unit vector along the magnetic field direction [7]. The contributions of plasma to ϵ and μ are negligible compared to the ones given by QED up to $\sim 3000R_{NS}$, for typical magnetospheric conditions of a magnetar [104]. The indices of refraction of the two linear polarization modes hence will differ from each other, i.e. the vacuum becomes birefringent [4]. Such QED vacuum birefringence decouples the polarization modes in the magnetosphere; therefore, the evolution of photon polarization will follow the magnetic field direction up to a large distance from the stellar surface [105]. The electric field associated to a photon of energy $\hbar\omega$ can be written in terms of its complex amplitude A as:

$$\vec{E} = \vec{A}(z)e^{i(k_0 z - \omega t)}, \tag{3.34}$$

where $k_0 = \omega/c$ [7]. Solving the wave equation it can be seen that the complex amplitude varies (along the photon trajectory) on a scale length $l_A \sim 1/k_0\delta \propto B^{-2}$, where $\delta =$

$(\alpha_F/45\pi)(B/B_Q)^2$ with α_F the fine structure constant. Comparing the latter scale length with the one over which the external magnetic field varies, namely $l_B = B/|\hat{k} \cdot \vec{\nabla} B| \sim r$, with r the radial distance [102], three different polarization evolution regimes can be identified. Near the surface, where B is large, it is $l_A \ll l_B$; so, the wave electric field can instantaneously adapt its direction to the variation of the local magnetic field direction; hence, photons maintain their original polarization state (either X or O) and are therefore said to propagate adiabatically. As they move away from this adiabatic region and from the stellar surface, the strength of the magnetic field decreases, so l_A increases more rapidly than l_B, and, at a certain point, it becomes comparable to it. In this intermediate region, the variation of the magnetic field can not be followed promptly by the wave electric field, so, at this point, the electric field direction freezes and it is not locked anymore to the one of the local magnetic field [105][4]. This occurs at a distance called adiabatic radius r_a in [102], or polarization radius, r_{pl}, in previous literature (e.g. [4][7]), defined implicitly by the condition $l_A = l_B$, that for typical parameters of a magnetar gives $r_a \sim 150 R_{NS}$ [104]. The adiabatic radius depends on both the photon energy and the star magnetic field: it is larger for stars with stronger magnetic field, and, at fixed B, it becomes smaller for less energetic photons [102]. The RCS of photons takes place at a radial distance $r_{\mathrm{RCS}} \lesssim 10 R_{NS}$, so for magnetars it is possible to treat the effects that RCS and QED have on polarization separately, given that $r_a \gg r_{\mathrm{RCS}}$ [7]. Finally, in the external region $l_A \gg l_B$ is found, so the electric field direction freezes and the polarization modes change as the magnetic field direction varies along the photon trajectory.

Mode switching

The polarization state of seed thermal photons can be further modified during their propagation in the magnetosphere, either through resonant scattering, or by the effects of vacuum polarization [7][105]. In the first case, evaluating the expression for the RCS cross section, it results that there is a higher probability that an O-mode photon is scattered into an X-mode one, instead a photon polarized in the X-mode is more likely to retain its initial polarization state [53]. In fact, the expressions for the (total) scattering cross section for the two modes are:

$$\sigma_{O-O} = \frac{1}{3}\sigma_{O-X} \qquad \sigma_{X-X} = 3\sigma_{O-X}. \tag{3.35}$$

In the second case, the so-called mode conversion of X-ray photons would be induced from a Mikheyev–Smirnov–Wolfenstein resonance of the vacuum, resulting from vacuum polarization [106]. The vacuum resonance point is related to the photon energy [56], and for X-ray photons it lies outside the photospheres of both X- and O-mode when $B \lesssim 7 \times 10^{13}$ G, therefore both X- and O-mode photons will undergo mode conversion at the vacuum resonance point and will escape as soon as they are produced. If this is the case, the seed thermal radiation will be mostly polarized in the O-mode, into which the originally dominant X-mode is converted. In contrast, when $B \gtrsim 7 \times 10^{13}$ G, the vacuum resonance is still located outside the X-mode photosphere but now lies inside the O-mode one [107], e.g. figure 3.8. This time, when X-mode photons are transformed into O-mode ones at the vacuum resonance point, since the latter is located inside the O-mode photosphere, they can not escape immediately and have to diffuse out until they reach the O-mode photosphere. Instead, O-mode photons converted into X-mode ones can escape immediately after their production, since matter is transparent for them

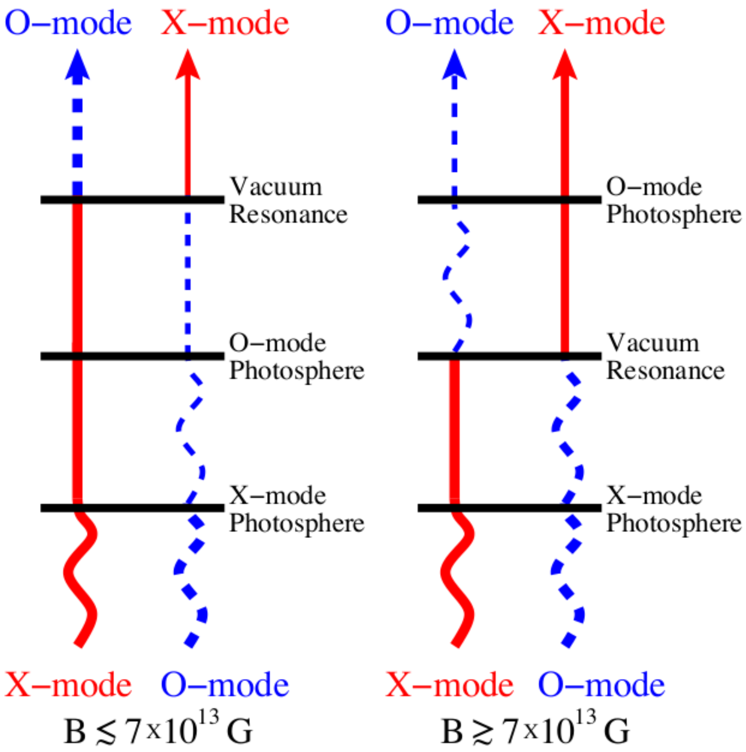

Figure 3.8: The vacuum polarization mode conversion effect on the thermal surface radiation is represented through a schematic diagram. The photospheres are defined as the point where the photons decouple from the matter, and they are located where the optical depth (measured from the surface) is 2/3. Here a complete adiabatic conversion is assumed across the vacuum resonance. Image taken from [109]

there; as a result, the dominant mode will still be the X-mode in this case [107]. For the conversion to be effective, the adiabatic condition must be satisfied:

$$E \gtrsim E_{\rm ad} = 1.49(f \tan\theta_k |1-u_i|)^{2/3} \left(\frac{5\ \rm cm}{H_\rho}\right)^{1/3}\ \rm keV, \tag{3.36}$$

where $f = f(B)$ is a slowly varying function of B of order unity, $u_i = (E_{c,p}/E)^2$, and $H_\rho = |{\rm d}z/{\rm d}\ln\rho|$ is the density scale height [108].

Chapter 4

Numerical implementation

The aim of this chapter is to describe the analysis of the data obtained from the polarimetric observations of the magnetar AXP 4U 0142+61, and the numerical implementation of the models that we computed in order to fit those data. The IXPE telescope is also described.

4.1 Observational data

4.1.1 IXPE

The Imaging X-ray Polarimetry Explorer (IXPE), a NASA Small Mission in collaboration with the Italian Space Agency (ASI), it was launched on 2021 December 9^{th} and it has opened a new window in X-ray polarimetry [1]. In fact, it combines polarimetry along with imaging, spectroscopic and timing capabilities [110]. It operates in the 2–8 keV energy range, it has a < 100 μs time resolution and a $> 11'$ field of view, along with a $\leq 30''$ half-energy width angular resolution.

Polarization measurements in the X-ray energy range are a powerful tool that allows to investigate a variety of astrophysical sources, such as AGN, radio pulsars and pulsar wind nebulae, supernova remnants, accreting X-ray pulsars, and magnetars. In particular, for synchrotron emitting sources an energy-dependent polarization map could offer an unprecedented insight on the magnetic-field structure of the X-ray emitting regions [111], or in magnetars, where vacuum birefringence, predicted by QED, produces a measurable effect on the polarization observables.

The IXPE observatory is made of three identical and co-aligned telescopes, each consisting of a mirror module assembly (MMA) [112], comprised of 24 concentrically nested mirror shells, with a polarization-sensitive imaging X-ray detector unit (DU) [113] at the focus, and of a coilable boom, deployed on orbit, necessary to provide the 4-m focal length to the conventional grazing incidence X-ray optics, based on Nickel-Cobalt alloy. The heart of the IXPE payload are the DUs, which provide position and energy determination, timing information, and, most importantly, polarization sensitivity. Inside of each DUs there is a Gas Pixel Detector (GPD), developed at INFN-Pisa and INAF-IAPS Rome [114], which makes possible polarimetry based on photoelectric effect at a few keV energy range. The photoelectric effect is the dominant interaction process for 2–8 keV photons and it is very sensitive to polarization. When a photon is absorbed in a gas gap emitting a photoelectron, this electron is ejected from an inner shell and it has a kinetic energy that is equal to the difference between the photon energy and the binding energy. The distribution of the photoelectron emission directions is not uniform, but it is peaked around that of the electric field of the photon, i.e. the polarization direction. After ejection, the photoelectron interacts with the surrounding gas, which slows it down through ionizing collisions with the atomic electrons, and it is scattered by Coulomb diffusion on the nuclei up to the point where it eventually stops. The absorber is left with a string of ionization (made by electron/ion pairs), which marks the path from the photoelectron creation at the original X-ray interaction site to its stopping point, the so-called "track". In the initial part of this track, the initial emission direction and the initial interaction point provide the polarization of the photon and the location of the absorption, respectively; whereas the total charge in the track provide the energy of the absorbed X-ray photon. The measured modulation curve, that is the histogram of the azimuthal emission direction distribution of the photoelectrons, is connected to the polarization observables. In fact, its amplitude is proportional to the PD and to the modulation factor μ (the amplitude of the instrumental response to completely polarized photons), while it shows a cosine square modulation, the phase of which allows to infer the polarization angle. In the case of IXPE, an X-ray enters through a beryllium window and interacts in the dimethyl ether (DME) gas mixture, which has a small diffusion coefficient and helps to maintain the information of the track. Such photoelectron track, then, drifts through a gas electron multiplier (GEM) to provide charge gain (typically ~ 200), the differential voltage on the GEM induces electron multiplication, and then onto a pixel anode readout, which makes a detailed image of the track.

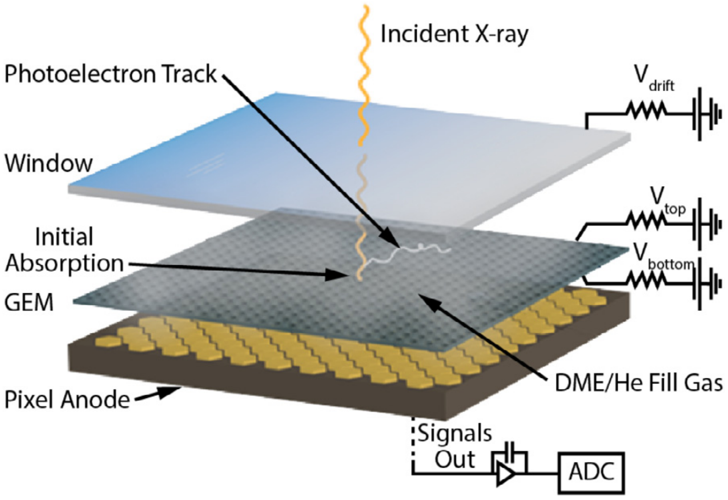

Figure 4.1: Schematic representation of the working principle of the polarization-sensitive GPD. Image taken from [1]

4.1.2 Data collection

IXPE observed the magnetar AXP 4U 0142+61 for a total of 840 ks between $2022-01-31$ and $2022-02-27$. We started our analysis from the background-subtracted photon lists, one for each DU. To extract the data the IXPEOBSSIM tools `xpselect` and `xpbin` have been used, a simulation and analysis suite specifically developed for IXPE [115]. The source counts and the background were extracted, respectively, from the region of interest (roi), which is a circular region with radius $46''$, and from a concentric annulus with inner and outer radius of $106''$ and $293''$, (see figure 4.2); the histograms

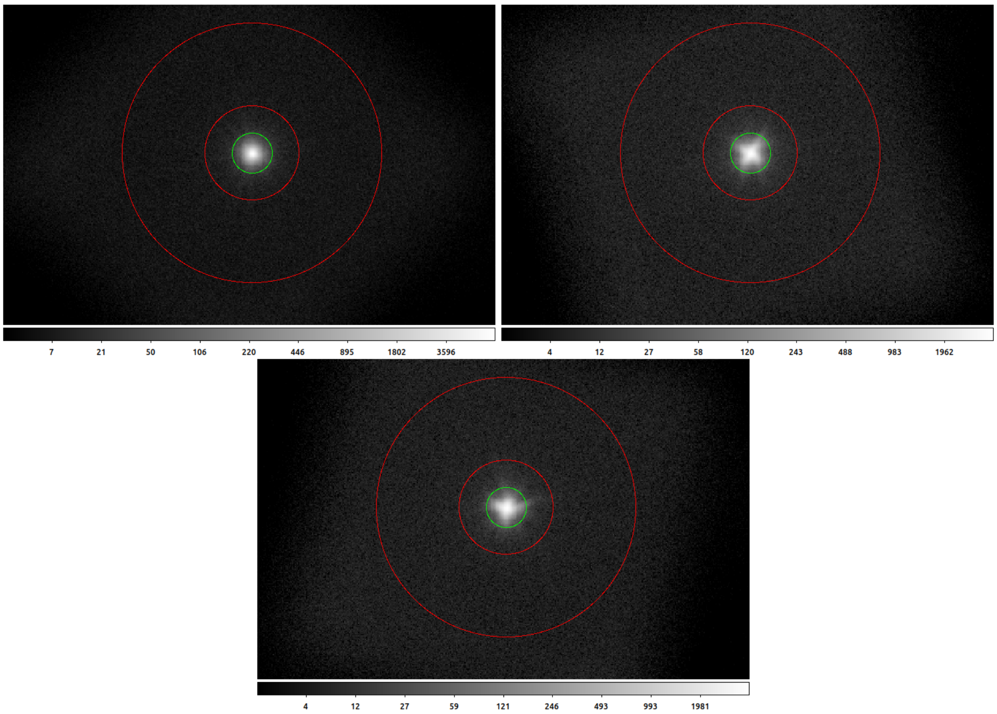

Figure 4.2: Extraction region for the source counts (green circles) and for the background counts (red annuli). The background has been highlighted using a logarithmic gray scale. Regions were selected with SAOIMAGEDS9. Image taken from [5]

for each of the three DU are shown in figure 4.3. As it can be seen, the first DU is more efficient than the other two by about $\sim 20\%$. Pulsations were detected with a frequency $f = 0.11507933$ Hz and a frequency derivative $\dot{f} = -2.1 \times 10^{-14}$ Hz s^{-1}. The energy range selected for the extraction of the data was 2–8 kev, further divided into 5 energy bins, and, in order to perform a phase-dependent analysis, the flux was sampled with 9 phase bins. The `pcube` fits files are then created, which contain the values of the Stokes parameters I, Q and U of the source and of the background, as well as the values of PD and PA, for each phase and energy bin and for each DU; the contributions of each DUs were then consistently summed together. The results of the phase-integrated analysis can be seen in table 4.1 and in figure 4.4, where the different behaviour between photons with energy $E \lesssim 4.5$ keV and $E \gtrsim 4.5$ keV for PD and PA is evident. Moreover, MDP$_{68}$ MDP$_{95}$ and MDP$_{99}$ are also shown for each energy bin in the PD plot[1], where $MDP_C = \sigma\sqrt{-2\ln(1-C)}$ with C the confidence level, i.e. either 68, 95, or 99%, and σ the 1σ error [116]. It has been suggested that the values of PD ($\sim 15\%$ between 2–3.5 keV, $< 9\%$ between 3.5–4.5 keV, $\sim 25\%$ between 6–8 keV) together with the swing of 90° in the PA at ~ 4.5 keV could be explained by a change in the dominant polarization mode of photons (see section 3.6.2) [5]. In this hypothesis, the low PD in the range $E \sim 2$–3.5 keV would point to a thermal emission from a condensed surface with photons mainly polarized in the O-mode, while the higher PD at higher energies would result from RCS in the magnetosphere, which would produce

---

[1] These quantities represent the Minimum Detectable Polarization, which provides the significance of the measurement: when the instrument measures a PD>MDP$_{99}$, it means that the signal is significant at a 99% CL (analogously for MDP$_{95}$ and MDP$_{68}$).

X-mode photons, as illustrated in figure 4.6. In fact, we can see in figure 3.6 that the emission from an atmosphere would lead to a much higher PD, whereas the condensed surface emission (see figure 3.7) has a PD closer to the one inferred from the data; the latter though is a bit higher, since it comes from an equatorial belt with a particular viewing geometry. The phase-dependent flux, PD and PA are instead illustrated in table 4.2 and in figure 4.5.

Bin	Flux (counts/cm^2/s)	PD	PA (deg)	MDP$_{68}$	MDP$_{95}$	MDP$_{99}$
2.0–2.6 keV	15265.60 ± 24.33	0.1376 ± 0.0118	180.000 ± 2.284	0.0178	0.0288	0.0358
2.6–3.5 keV	8680.71 ± 20.63	0.1610 ± 0.0110	180.387 ± 2.989	0.0166	0.0270	0.0335
3.5–4.6 keV	3666.05 ± 17.49	0.0873 ± 0.0179	180.597 ± 3.920	0.0271	0.0439	0.0544
4.6–6.0 keV	1300.05 ± 14.77	0.1330 ± 0.0371	84.418 ± 5.187	0.0560	0.0909	0.1127
6.0–8.0 keV	630.71 ± 18.61	0.2672 ± 0.0837	92.140 ± 6.985	0.1263	0.2048	0.2540

Table 4.1: The energy-dependent data extracted from the source.

Bin	Flux (counts)	PD	PA (deg)	MDP$_{68}$	MDP$_{95}$	MDP$_{99}$
0.001–0.699 keV	3452.550 ± 15.124	0.0998 ± 0.0232	63.998 ± 6.651	0.0350	0.0567	0.0703
0.699–1.397 keV	3090.680 ± 14.346	0.1022 ± 0.0246	30.866 ± 6.893	0.0371	0.0602	0.0746
1.397–2.095 keV	2918.710 ± 13.577	0.1111 ± 0.0250	39.941 ± 6.447	0.0377	0.0611	0.0758
2.095–2.794 keV	3104.569 ± 13.997	0.1491 ± 0.0243	30.929 ± 4.674	0.0367	0.0595	0.0738
2.794–3.492 keV	3274.979 ± 14.405	0.1319 ± 0.0236	41.952 ± 5.132	0.0357	0.0578	0.0717
3.492–4.190 keV	3303.100 ± 14.390	0.1623 ± 0.0233	36.720 ± 4.117	0.0352	0.0571	0.0708
4.190–4.888 keV	3221.145 ± 14.456	0.1222 ± 0.0239	54.802 ± 5.613	0.0361	0.0586	0.0726
4.888–5.586 keV	3535.908 ± 14.811	0.1599 ± 0.0224	56.874 ± 4.015	0.0338	0.0548	0.0680
5.586–6.284 keV	3641.468 ± 15.156	0.1484 ± 0.0222	69.478 ± 4.291	0.0336	0.0544	0.0675

Table 4.2: The phase-dependent data extracted from the source.

4.2 Numerical modelling

The models that we computed rely on the assumption that the magnetic field of the source is a globally twisted dipole, characterized by the twist angle $\Delta\phi$ which measures the amount of shear between two footpoints of a closed magnetic field line. Moreover, we assumed that the currents circulating along the closed field lines are described by the unidirectional flow model, so currents are formed only by electrons streaming from the northern to the southern magnetic hemisphere. Their velocity is a superposition of a Maxwellian distribution at a temperature $kT_e = 10$ keV and of the speed β along the closed magnetic field lines (as discussed in section 3.4). Thermal seed photons then undergo resonant Compton scatterings (RCS) onto these charges in the magnetosphere. Pair creation is neglected in our framework, since a self-consistent model capable of

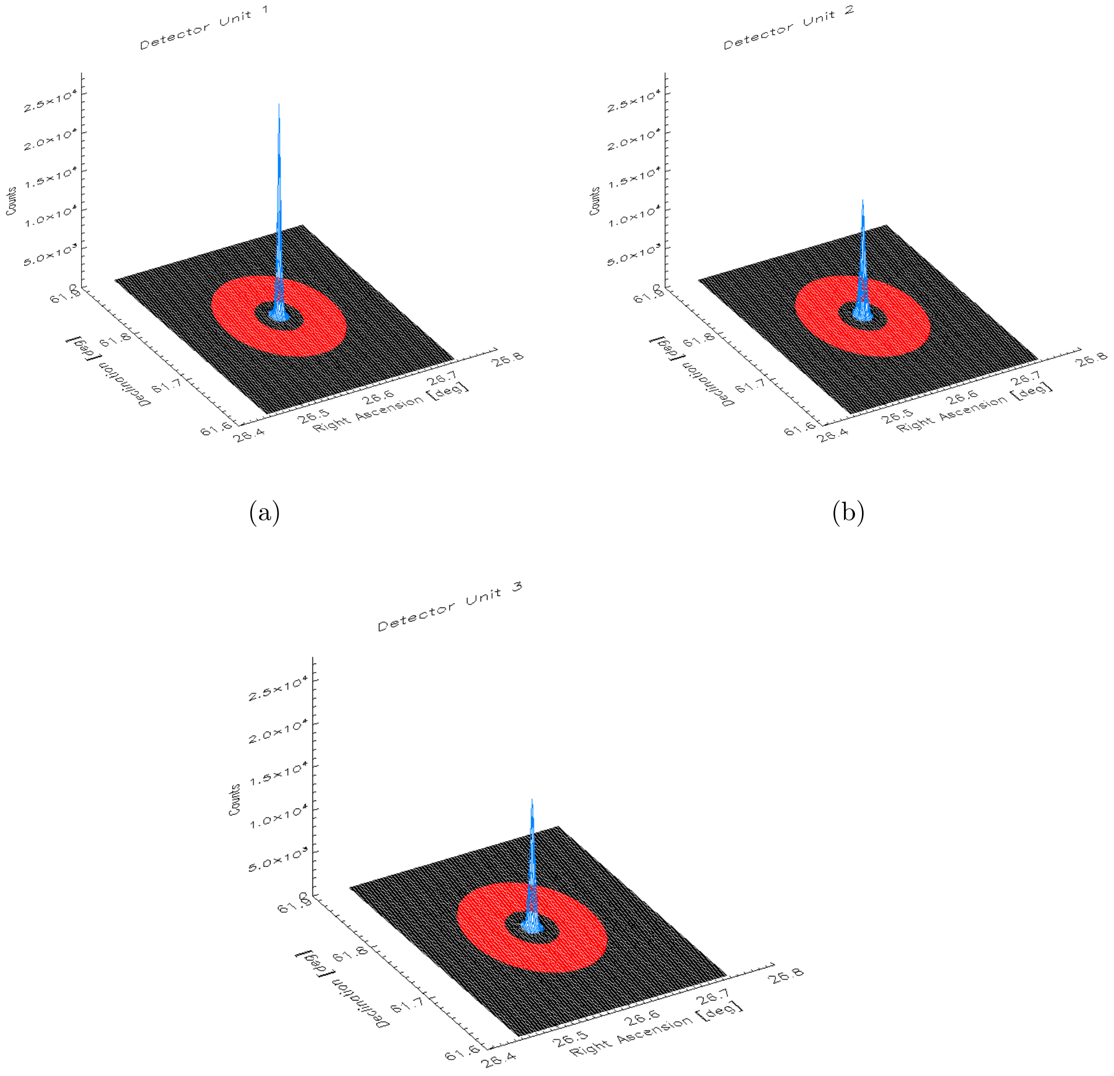

(a) (b)

(c)

Figure 4.3: Histograms of the total number of counts revealed by DU 1 (a), DU 2 (b), and DU 3 (c). The source counts from the roi region are marked in light blue, while the background ones from the annulus in red.

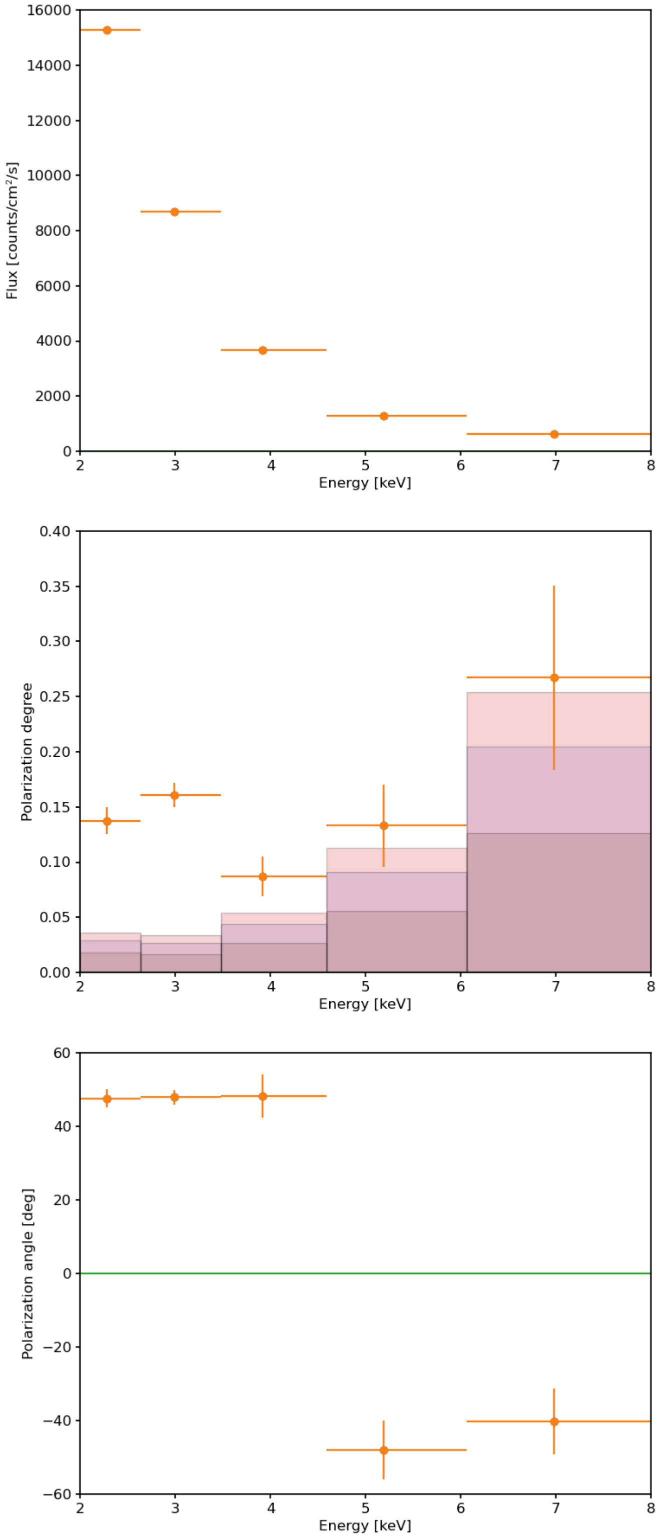

Figure 4.4: Flux (top), PD (middle), and PA (bottom) as a function of energy, for the IXPE observation of the AXP 4U 0142+61. Background subtracted data are represented in orange. MDP_{68}, MDP_{95}, and MDP_{99} are also shown in the middle plot.

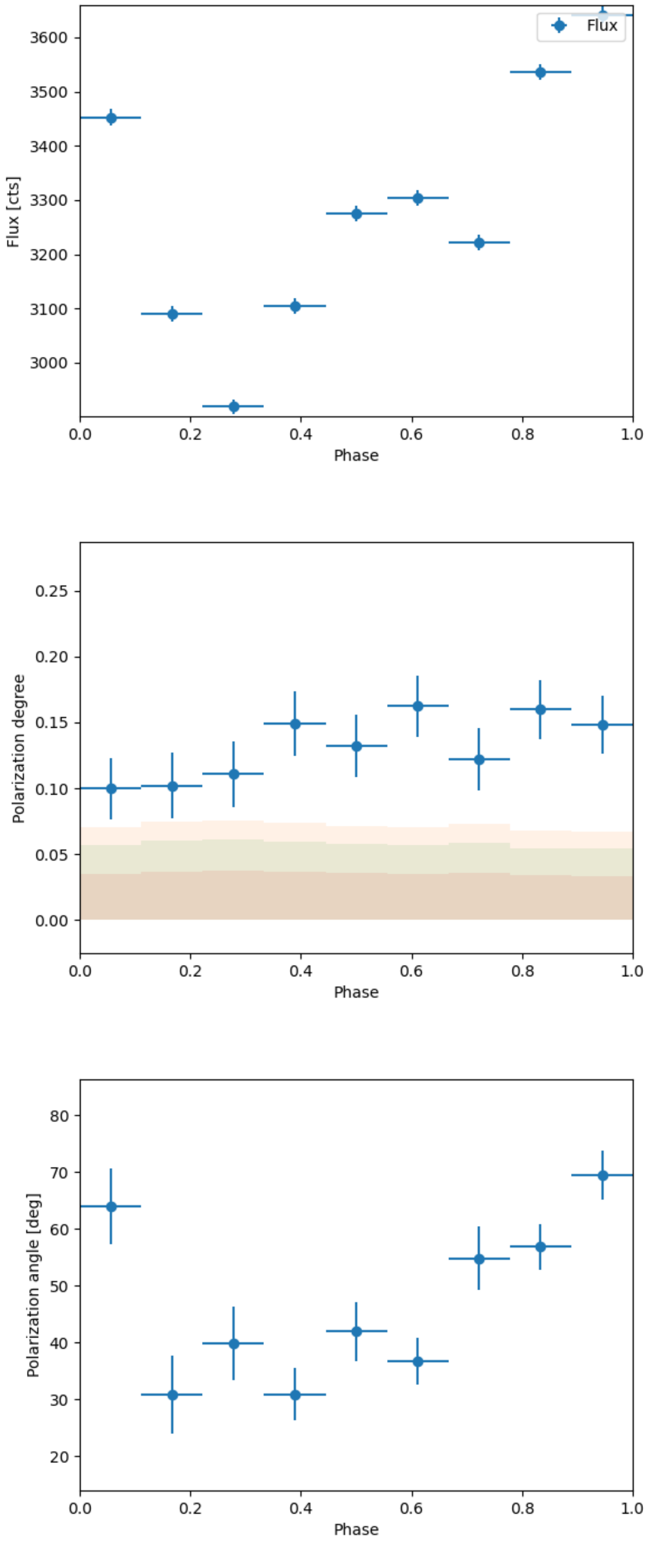

Figure 4.5: Flux (top), PD (middle), and PA (bottom) as a function of the phase, for the IXPE observation of the AXP 4U 0142+61. In the middle plot MDP_{68}, MDP_{95}, and MDP_{99} are also shown.

taking into account the contribution of $e^{\pm}$ pairs has not yet been developed. In addition, models were created either accounting for or neglecting QED effects, i.e. vacuum birefringence. The surface of the star is assumed to be composed by iron in a condensed

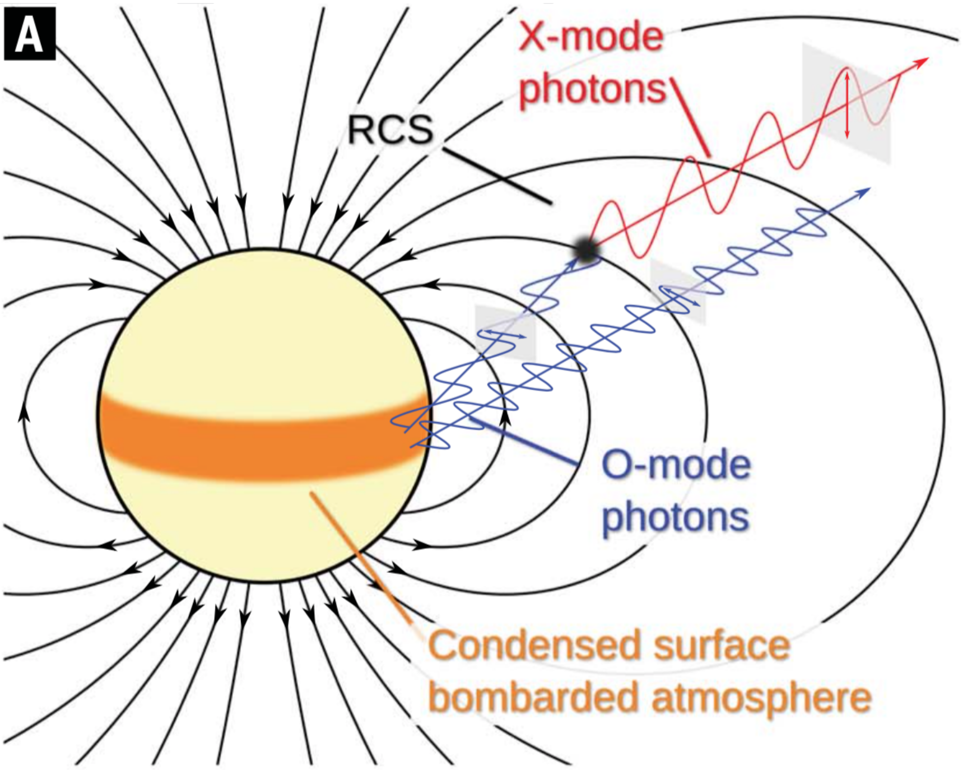

Figure 4.6: Condensed surface thermal radiation from an equatorial belt of a magnetar, further reprocessed by RCS in the magnetosphere. The emitting region is the orange one, the (dipole) magnetic field lines are represented by the black lines with arrows, the grey rectangles highlight the polarization plane along the photon trajectories, and the blue and red arrow indicate the direction of the oscillating electric field. Image taken from [5], where a bombarded atmosphere was also considered as a possible surface emission model.

state in either the fixed- or free-ion limit, with a hotter belt close to the magnetic equator (see figure 4.6), following a previous analysis of this same source [5], where a hotter, continuous equatorial belt successfully reproduced the energy-dependent data. However, at variance with the latter work, we assumed that such a belt is limited in azimuth, because a continuous one could not fit the phase-dependent data. As it will be discussed in the next chapter, even considering an azimuthal-limited equatorial belt we were not able to reproduce well the data when performing a simultaneous fit of the light curve, PD, and PA; therefore, we also considered antipodal hotter spots on the magnetar surface. The emission of the star is modeled by dividing its surface into a number of patches through a 10×10 angular grid, where each patch is identified by the magnetic colatitude Θ and by the azimuth Φ of the patch centre. To compute our set of different models we assumed that these surface patches emit at a temperature $kT_{\rm cold} \sim 50$ eV everywhere but on the equatorial belt or on the antipodal spots, where three different temperatures were chosen, namely $kT_{\rm hot} = 0.35, 0.45, 0.55$ keV. Furthermore, for each temperature and for each emission geometry, we also fixed a value for $\Delta\phi$, which is assumed to vary between 0.0 (no twist) and 0.5 radians with a step of 0.1.

Another free parameter is the velocity β of the charges (in units of c) along the closed field lines, ranging from 0.1 to 0.6 with a step of 0.1. Each patch of the surface emits 80000 photons, so that, in the end, the total number of collected photons is of the order of 10^7. The reprocessing of these photons by the magnetospheric charges is accounted for by means of a Monte Carlo simulation [7][3]; both the scattered and the unscattered photons are collected on the so-called sky at infinity. The latter is a sphere composed by a 15×15 angular grid (Θ_s, Φ_s), similarly to what has been done for the stellar surface. A photon is emitted by the star, then is reprocessed (or not) by the magnetosphere and is collected by one of the patches of the sky at infinity, located at a large distance from the star (and its magnetosphere), allowing us to consider the source as point-like. The geometry of the star is accounted for by means of the angles χ, ranging from $0.1°$ to $179.9°$ with a step of $15°$, and ξ, in the range $[0°, 89.9°]$ also with a step of $15°$ (see section 2.2 and figure 2.1). They are incorporated using an IDL script, which, for a given value of χ and ξ, selects the patches of the sky at infinity that would receive the escaping photons from the portion of the star that is "in view" at that phase. No general relativity (GR) correction, light bending and gravitational redshift, is accounted for. In the magnetar case, however, this effect is likely to be less relevant, since a sizable part of the thermal photons emitted from the surface will scatter at $\sim$ 5–10 stellar radii before reaching infinity, and at that point the influence of GR effects is reduced. In fact, Fernández and Davis [104] obtained a good agreement between results of the Monte carlo code accounting or not for GR effects. Moreover, GR could also influence the polarization state of photons, rotating the polarization plane along null geodesics [117], but these effects are negligible compared to the QED ones [3]. The values of the Stokes parameters I, Q and U (see section 3.6.1) are hence obtained, for each of the 9 phase bins and for each of the 5 energy bins. In order to perform a phase-dependent analysis, in each phase bin the Stokes parameters are summed and integrated over the energy band (2–8 keV) to find the flux, PD and PA.

Chapter 5

Results

In this chapter we are going to describe the results we obtained from the fit of the real source data with the synthetic models, either an equatorial belt or two antipodal spots. This fit was carried out through a python script, which takes in input the phase-dependent, collected data of the source and a model of our choice between either fixed or free ions, and either including or not QED effects. The computed models, as we saw, are further characterized by a certain number of free parameters, given by χ, ξ, $\Delta\phi$, β, T. To these parameters we have to add a normalization factor, due to the fact that the total number of photons in the synthetic models is $\sim 10^7$ but the real number of photons collected by IXPE is much lower; moreover, we also add a shift of the polarization angle, because the one inferred from IXPE is measured with respect to the preferential axis of the telescope (pointing towards the celestial North Pole), while in the synthetic models PA is measured with respect to the star rotation axis projected in the plane of the sky. Either a single or a simultaneous fit of the flux, PD and PA can be performed; in the case of a simultaneous fit, two quantities can be fitted as well as the three of them. Finally, it does a multilinear interpolation in the multidimensional space of the free parameters, and searches for a local minimum of the parameters hypersurface using the χ^2 statistic.

5.1 Equatorial belt

At first, as we said in the previous chapter, we started with a hotter, azimuth-limited equatorial belt on a condensed surface in either the fixed- or free-ions limit. In particular, we started by fitting the observed light curve with a model composed by a belt with an extension of $\sim 35° \times 250°$ (model (A)); then, we also performed a simultaneous fit of the polarization observables, PD and PA. At this point, we simultaneously fitted the flux along with PD and PA, but a condensed surface neither in the fixed- nor in the free-ions limit could provide a successful fit, not even trying to fix some parameters. In fact, as it can be seen in table 5.1 the best fit we obtained was for a condensed surface in the fixed-ions limit and had $\chi^2_{\text{red}} = 26.5$ (in figure 5.1 the plot of this fit). Consequently, we tried to fit the observed light curve still with a hotter equatorial belt on a condensed surface either in the fixed- or free-ions limit, but this time we considered a smaller portion of such belt, with an extension of about $35° \times 70°$, and a larger one $\sim 35° \times 110°$, separated by $\sim 100°$ in longitude (model (B)). The next step consisted, as before, in the simultaneous fit of PD and PA, followed by the simultaneous fit of all the three observables, flux, PD and PA. Neither this last fit produced a better result,

	χ (deg)	ξ (deg)	$\Delta\phi$ (rad)	β	T	χ^2_{red}
Input values	169.9	67.1	0.50	0.57	0.45	–
Belt (A)						
(flux+PD+PA)						
QED-ON	169.9[1]	67.1[1]	0.50[2]	0.58 ± 0.01	0.43 ± 0.01	26.5

Table 5.1: Results of the simultaneous fit of flux, PD and PA between the data and a model consisting of a condensed surface in the fixed-ions limit with a hotter equatorial belt with an extension ~ 35° × 250°.

	χ (deg)	ξ (deg)	$\Delta\phi$ (rad)	β	T	χ^2_{red}
Input values	151.3	2.4	0.50	0.52	0.45	–
Belt (B)						
(flux+PD+PA)						
QED-ON	165.0 ± 1.3	0.1[3]	0.50 ± 0.03	0.60 ± 0.01	0.55 ± 0.01	98.5

Table 5.2: Results of the simultaneous fit of flux, PD and PA between the data and a model consisting of a condensed surface in the fixed-ions limit with a hotter smaller portion of the equatorial belt with an extension of about 35° × 70°, and a larger one ~ 35° × 110°, separated by ~ 100° in longitude.

with $\chi^2_{\text{red}} = 98.5$ for a condensed surface in the fixed-ions limit, as reported in table 5.2 and in figure 5.2.

5.2 Antipodal spots

The second attempt to find a suitable model was to consider antipodal hotter spots on the magnetar condensed surface, once again either in the fixed- or free-ions limit. Proceeding analogously to what we did for the equatorial belt case, we started by fitting the observed light curve alone with a model formed by a larger, hotter spot in the northern hemisphere of the source, located about 45° from the spin axis and with an extension of ~ 35° × 100°, and a smaller one of ~ 35° × 70° for the antipodal hotspot in the southern hemisphere. The best fit model was obtained from a condensed surface in the free-ions limit. The next step, as in the previous case, consisted in the simultaneous fit of the polarization observables, PD and PA. The best fit values were found choosing as initial values of the parameters those found after the single fit of the observed flux; the results and plot can be seen, respectively, in table 5.3 and in figure 5.3. Such a rather high value of the χ^2_{red} is not surprising, considering that the possible values of the parameters in the produced synthetic models were quite a few (for instance, the angles χ and ξ vary with a step of 15°), in order to reduce the computational time to produce such models. Finally, the simultaneous fit of the light curve, PD and PA was performed, and, once again, the best fit was achieved using as initial values of the parameters the ones resulting from the fit of the light curve. The fit obtained considering the antipodal spots model turns out to be far better than the one resulting using an

---

[1] This parameter was fixed during the fit

[2] This parameter hit the upper bound value of the range during the fit

[3] This parameter hit the lower bound value of the range during the fit.

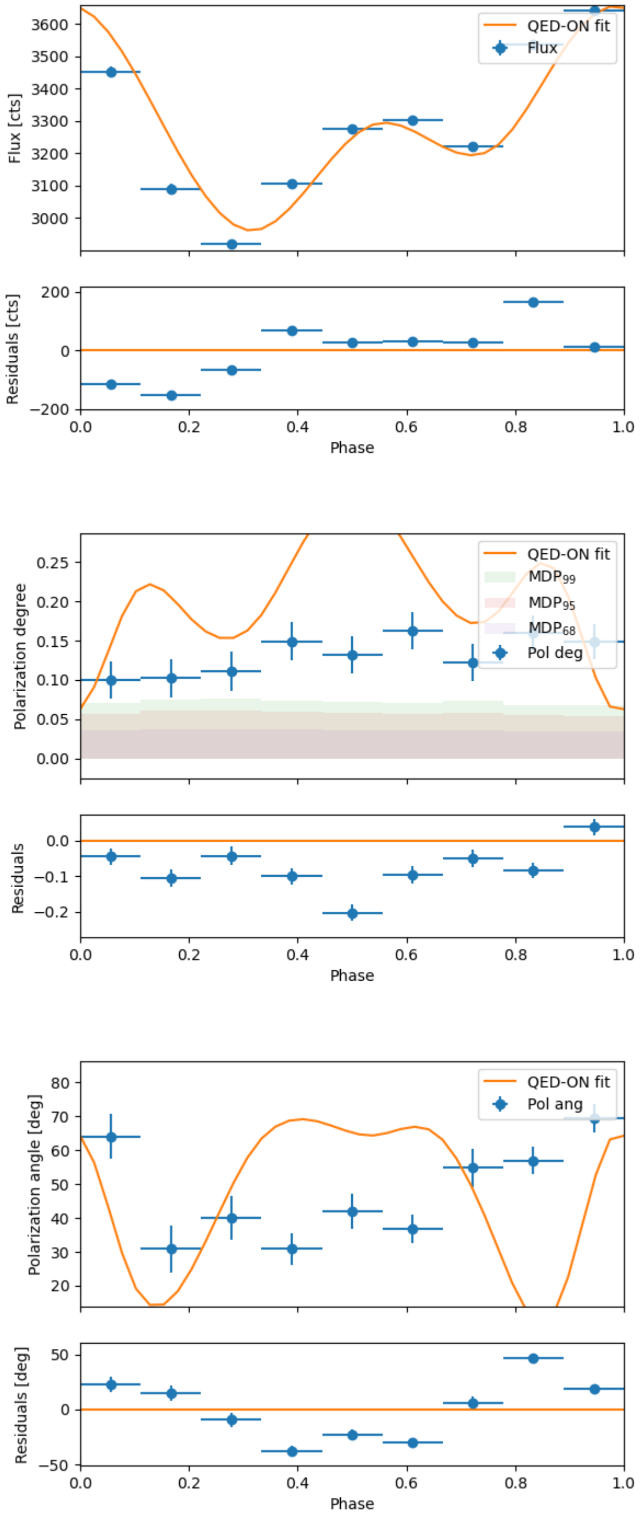

Figure 5.1: Flux (top), PD (middle), and PA (bottom) as a function of the phase, fitted with a model which consists of a condensed surface in the fixed-ions limits with a continuous hotter belt with an extension $\sim 35^\circ \times 250^\circ$, fixing the values of χ and ξ. In the middle plot MDP_{68}, MDP_{95}, and MDP_{99} are also shown.

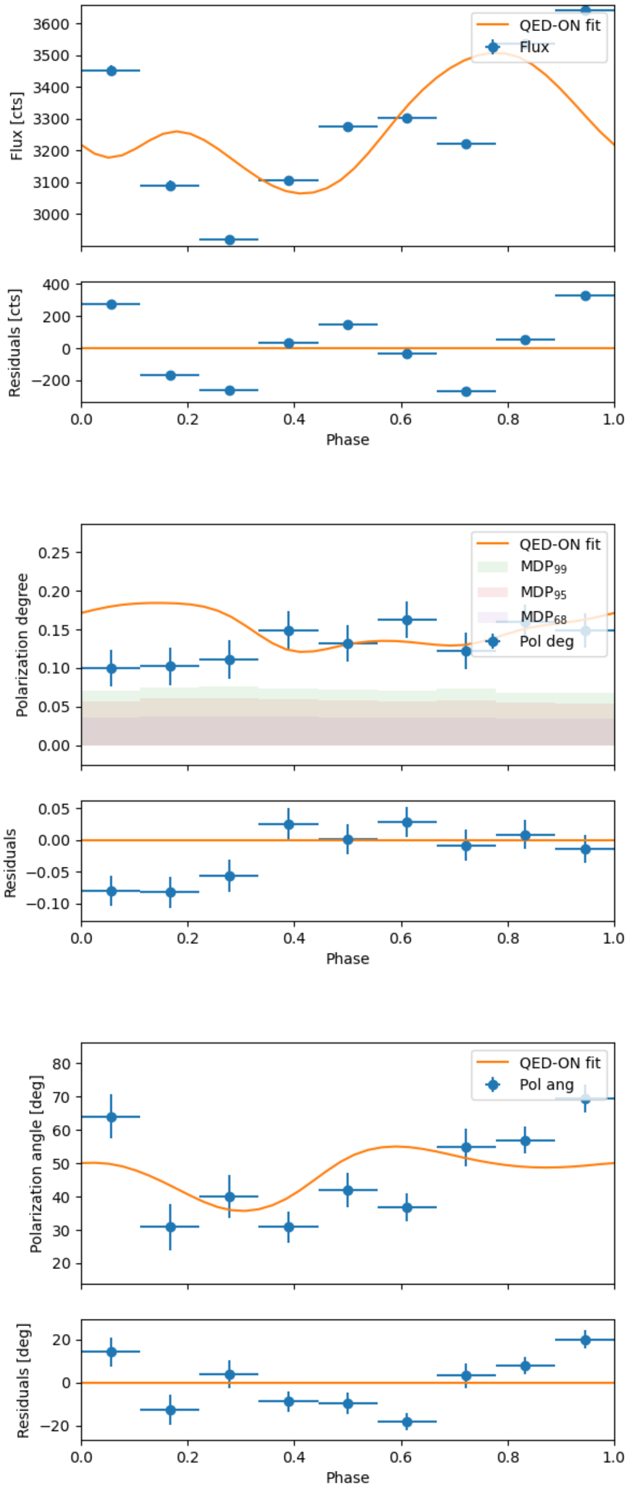

Figure 5.2: Flux (top), PD (middle), and PA (bottom) as a function of the phase, fitted with a model consisting of a condensed surface in the fixed-ions limit with a hotter smaller piece of the equatorial belt with an extension of about 35° × 70°, and a larger one ∼ 35° × 110°, separated by ∼ 100° in longitude. In the middle plot MDP_{68}, MDP_{95}, and MDP_{99} are also shown.

	χ (deg)	ξ (deg)	$\Delta\phi$ (rad)	β	T	χ^2_{red}
Input values	12.4	46.2	0.44	0.10	0.48	–
Antipodal						
(PD+PA)						
QED-ON	10.0 ± 1.8	35.1 ± 5.5	0.35 ± 0.05	0.20 ± 0.07	0.45 ± 0.15	4.5
QED-OFF	0.1 ± 0.9	44.4 ± 475.4	0.40 ± 10.92	0.10 ± 4.83	0.52 ± 5.28	11.2

Table 5.3: Results of the simultaneous fit of PD and PA between the data and a model consisting of a condensed surface in the free-ions limit with two antipodal hotter spots, extended $\sim 35^\circ \times 100^\circ$ in the northern hemisphere and located about 45° from the spin axis, and an extension of $\sim 35^\circ \times 70^\circ$ in the southern one, either accounting or not for QED effects.

	χ (deg)	ξ (deg)	$\Delta\phi$ (rad)	β	T	χ^2_{red}
Input values	12.4	46.2	0.44	0.10	0.48	–
Antipodal						
(flux+PD+PA)						
QED-ON	12.0 ± 0.4	45.3 ± 0.2	0.50^2	0.11 ± 0.01	0.47 ± 0.01	6.1
QED-OFF	15.0 ± 0.8	45.0 ± 0.7	0.31 ± 0.01	0.37 ± 0.01	0.48 ± 0.01	20.5

Table 5.4: Same as table 5.3, but for the simultaneous fit of flux, PD and PA.

equatorial belt, with a $\chi^2_{\text{red}} = 6.1$ for the former and a $\chi^2_{\text{red}} = 26.5$ for the latter. Once again, we found quite a high value of χ^2_{red}, and a possible cause could be the very small error bars displayed in the plot of the flux (see top plot of figure 4.5), therefore we expect higher values for the χ^2_{red} even for rather successful fits. Moreover, the IXPE telescope is devoted to polarimetric observations, so its spectroscopic measurements are not fully reliable [1]. This, together with the aforementioned reasons, makes it difficult to attain the acceptable low values $\chi^2_{\text{red}} \simeq 1$. Then, we also performed a fit, following the same steps just described (with the plot of these fit in the same figures 5.3, and 5.4), for the same model but without taking into account the QED effects (QED-OFF), since we obtained a good result considering the vacuum birefringence of the magnetized vacuum in the magnetosphere (QED-ON). Confronting the results of these two fits (reported in the same tables 5.3, and 5.4), we can see that, as expected, the QED-ON fit is always better with respect to the QED-OFF one, i.e. $\chi^2_{\text{red,QED-ON}} = 4.5$ and $\chi^2_{\text{red,QED-OFF}} = 11.2$ for the simultaneous fit of the polarization observables, and $\chi^2_{\text{red,QED-ON}} = 6.1$ against $\chi^2_{\text{red,QED-OFF}} = 20.5$ for the simultaneous fit of flux, PD and PA.

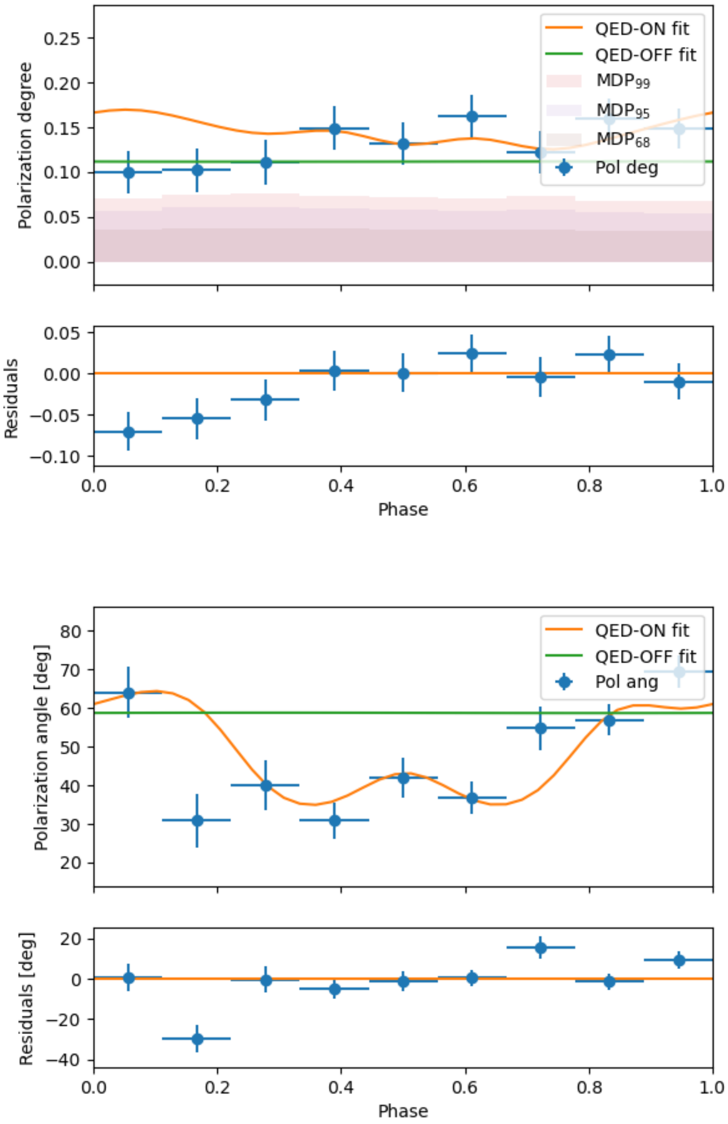

Figure 5.3: PD (top) and PA (bottom) as a function of the phase, simultaneously fitted with a model which consists of a condensed surface in the free-ions limit having two antipodal hotter spots, with an extension of ∼ 35° × 100° in the northern hemisphere located about 45° from the spin axis, and an extension of ∼ 35° × 70° in the southern one. The orange and the green solid lines refer to the QED-ON and QED-OFF model, respectively. In the PD plot MDP$_{68}$, MDP$_{95}$, and MDP$_{99}$ are also shown.

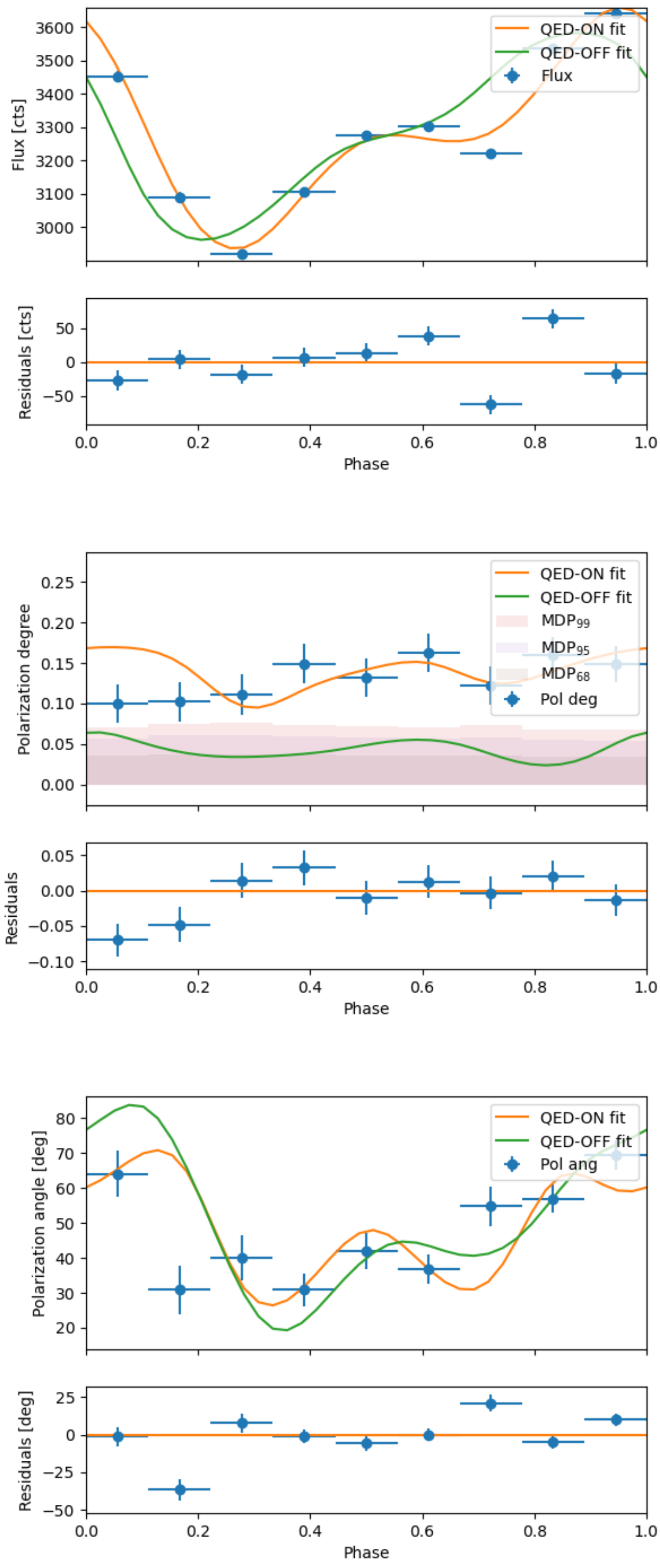

Figure 5.4: Same as figure 5.3, but for the simultaneous fit of flux (top), PD (middle), and PA (bottom). In the middle plot MDP_{68}, MDP_{95}, and MDP_{99} are also shown.

Chapter 6

Discussion and conclusions

In this work we analyzed and tried to model the X-rays polarization data observed by IXPE from the magnetar AXP 4U 0142+61. After having introduced the underlying theoretical model of magnetars, and discussed the spectral observations carried out so far, we described the numerical implementation of the surface emission model, including the transport of spectral and polarization properties to infinity; finally, we fit the IXPE data using an archive of theoretical models obtained from different values of the input parameters. When computing the synthetic models, some unavoidable simplifications were made; for instance, the so-called unidirectional flow approximation is used to describe the charges motion along the closed magnetic field lines in the magnetosphere, which means that we considered only the motion of the electrons, neglecting ions. Pair production was neglected as well, since a self-consistent model accounting also for the $e^{\pm}$ pairs contribution has not been developed yet. In addition, the magnetosphere was assumed to be globally twisted with a constant twist angle $\Delta\phi$, for simplicity; we have also considered the surface temperature as constant across the surface of the star.

The first analysis of IXPE data from this same source [5] was focused on the energy dependence of the polarization properties, in particular on the swing of the polarization angle by 90° observed at the energy $E \sim$ 4–5 keV. They were successfully fitted by a model characterized by an iron condensed surface with an emitting equatorial belt, whose radiation is further reprocessed by RCS in the magnetosphere. However, a continuous belt, alike that of the latter model, is hard to reconcile with the observed double-peaked light curve of the source. This led us to consider an azimuth-limited equatorial belt in the computation of the synthetic models; however, even the best-fit models, when fitting simultaneously the flux together with PD and PA, did not succeed in replicating the data, as can be seen in tables 5.1, 5.2, and in figures 5.1, 5.2. As a consequence, we tried to model the surface emission of the magnetar with two antipodal hotter spots, a larger one in the northern hemisphere, located about 45° from the spin axis and with an extension of $\sim 35^\circ \times 100^\circ$, and a smaller one of $\sim 35^\circ \times 70^\circ$ in the southern hemisphere. This model in the free-ions limit could fit quite well the data either performing a single fit of the light curve, a simultaneous one of the polarization observables, as well as a simultaneous fit of the flux, PD and PA. As already noticed in section 5.2, the χ^2_{red} are higher than what we would expect from a good fit ($\chi^2_{\text{red}} \simeq 1$). A possible cause could be the small error bars in the flux plot (figure 4.5), which are certainly underestimated, considering that IXPE is focused on polarization observations and is not guaranteed to provide precise spectroscopic measurements. On the other hand, the best fitting model is found interpolating between models with different values of the parameters, which vary on rather coarse grids, and, while a thicker grid might probably contribute to find best fitting models which would better reproduce the observed data, this would also lead to a tremendous growth of the computational times. We also tried to perform the same fits with the same model but with QED effects "switched off", and we saw that it did not fit successfully the observed data, i.e. $\chi^2_{\text{red,QED-ON}} = 6.1$ against $\chi^2_{\text{red,QED-OFF}} = 20.5$ for the simultaneous fit of flux, PD and PA. This is in agreement with the theoretical prediction, even if the observed polarization is too low ($\sim 20\%$) for a proper test of the presence of the the vacuum birefringence. In the end, we found that there exist at least one condensed surface model capable to explain the phase-dependent observed data.

IXPE observations have already opened a new era in the magnetar study. In addition to the observation of the magnetar AXP 4U 0142+61, IXPE observed also other two sources, namely SGR 1806−20 [118] and 1RXS J170849.0−400910 [119]. The former exhibits no significant PD, apart from the 4–5 keV energy range, with PD$= 31.6 \pm 10.5\%$ and PA$= -17^\circ.6^{+15^\circ.5}_{-15^\circ.0}$, due to the all-time-low persistent flux level during the observations; the latter, instead, showed a higher X-ray polarization with respect to the other two sources, with a PD increasing with the energy and without a swing by 90° in PA. This demonstrate that, even when the spectral model is similar (a blackbody plus a powerlaw for all the three sources), polarization measurements can disentangle the intrinsic degeneracy of RCS models. Polarimetric observations can give an unprecedented insight on the polarization processes happening in sources with such strong magnetic field both on the magnetar surface (the underlying emission model), as well as in the magnetosphere (RCS). In addition, they might lead to the first indirect evidence, so far only theoretically predicted, of the presence of QED effects, i.e. vacuum birefringence, in the magnetized vacuum around the star. IXPE mission was extended by 20 months, so future observations of magnetars might help us to take a leap forward in the comprehension of these sources, further constraining the possible surface emission model as well as their polarization properties.

Bibliography

[1] Martin C. Weisskopf et al. "The Imaging X-Ray Polarimetry Explorer (IXPE): Pre-Launch". In: *Journal of Astronomical Telescopes, Instruments, and Systems* 8.2, 026002 (Apr. 2022), p. 026002. DOI: `10.1117/1.JATIS.8.2.026002`. arXiv: `2112.01269 [astro-ph.IM]`.

[2] Robert C. Duncan and Christopher Thompson. "Formation of Very Strongly Magnetized Neutron Stars: Implications for Gamma-Ray Bursts". In: *Astrophysical Journal Letters* 392 (June 1992), p. L9. DOI: `10.1086/186413`.

[3] R Taverna, R Turolla, V Suleimanov, A Y Potekhin, and S Zane. "X-ray spectra and polarization from magnetar candidates". In: *Monthly Notices of the Royal Astronomical Society* 492.4 (Jan. 2020), pp. 5057–5074. DOI: `10.1093/mnras/staa204`. URL: `https://doi.org/10.1093%2Fmnras%2Fstaa204`.

[4] Jeremy S. Heyl and Nir J. Shaviv. "QED and the high polarization of the thermal radiation from neutron stars". In: *Physical Review D* 66.2 (July 2002). DOI: `10.1103/physrevd.66.023002`. URL: `https://doi.org/10.1103%2Fphysrevd.66.023002`.

[5] Roberto Taverna et al. "Polarized x-rays from a magnetar". In: *Science* 378.6620 (Nov. 2022), pp. 646–650. DOI: `10.1126/science.add0080`. URL: `https://doi.org/10.1126%2Fscience.add0080`.

[6] "Star Deaths and the Formation of Compact Objects". In: *Black Holes, White Dwarfs, and Neutron Stars*. John Wiley & Sons, Ltd, 1983. Chap. 1, pp. 1–16. ISBN: 9783527617661. DOI: `https://doi.org/10.1002/9783527617661.ch1`. eprint: `https://onlinelibrary.wiley.com/doi/pdf/10.1002/9783527617661.ch1`. URL: `https://onlinelibrary.wiley.com/doi/abs/10.1002/9783527617661.ch1`.

[7] R. Taverna et al. "Probing magnetar magnetosphere through X-ray polarization measurements". In: *Monthly Notices of the Royal Astronomical Society* 438.2 (Dec. 2013), pp. 1686–1697. DOI: `10.1093/mnras/stt2310`. URL: `https://doi.org/10.1093%2Fmnras%2Fstt2310`.

[8] R Turolla, S Zane, and A L Watts. "Magnetars: the physics behind observations. A review". In: *Reports on Progress in Physics* 78.11 (Oct. 2015), p. 116901. DOI: `10.1088/0034-4885/78/11/116901`. URL: `https://doi.org/10.1088%2F0034-4885%2F78%2F11%2F116901`.

[9] Werner Becker, Mike G. Bernhardt, and Alex Jessner. "Autonomous Spacecraft Navigation With Pulsars". In: *Acta Futura* 07 (2013), pp. 11–28. DOI: `10.2420/AF07.2013.11`. URL: `https://doi.org/10.2420/AF07.2013.11`.

[10] E. F. Keane and M. A. McLaughlin. “Rotating Radio Transients”. In: *Bulletin of the Astronomical Society of India* (2011). arXiv: `1109.6896 [astro-ph.SR]`.

[11] Davide De Grandis et al. “X-Ray Emission from Isolated Neutron Stars Revisited: 3D Magnetothermal Simulations”. In: *The Astrophysical Journal* 914.2 (June 2021), p. 118. DOI: `10.3847/1538-4357/abfdac`. URL: `https://dx.doi.org/10.3847/1538-4357/abfdac`.

[12] Ü. Ertan, Ş . Çalışkan, O. Benli, and M. A. Alpar. “Long-term evolution of dim isolated neutron stars”. In: *Monthly Notices of the Royal Astronomical Society* 444.2 (Aug. 2014), pp. 1559–1565. DOI: `10.1093/mnras/stu1523`. URL: `https://doi.org/10.1093%2Fmnras%2Fstu1523`.

[13] A. De Luca. “Central compact objects in supernova remnants”. In: *Journal of Physics: Conference Series* 932 (Dec. 2017), p. 012006. DOI: `10.1088/1742-6596/932/1/012006`. URL: `https://doi.org/10.1088%2F1742-6596%2F932%2F1%2F012006`.

[14] Sandro Mereghetti. “The strongest cosmic magnets: soft gamma-ray repeaters and anomalous X-ray pulsars”. In: *The Astronomy and Astrophysics Review* 15.4 (July 2008), pp. 225–287. DOI: `10.1007/s00159-008-0011-z`. URL: `https://doi.org/10.1007%2Fs00159-008-0011-z`.

[15] D. Viganò et al. “Unifying the observational diversity of isolated neutron stars via magneto-thermal evolution models”. In: *Monthly Notices of the Royal Astronomical Society* 434.1 (Sept. 2013), pp. 123–141. DOI: `10.1093/mnras/stt1008`. arXiv: `1306.2156 [astro-ph.SR]`.

[16] Victoria M. Kaspi. “Grand unification of neutron stars”. In: *Proceedings of the National Academy of Sciences* 107.16 (Apr. 2010), pp. 7147–7152. DOI: `10.1073/pnas.1000812107`. URL: `https://doi.org/10.1073%2Fpnas.1000812107`.

[17] Roberto Turolla. “Isolated Neutron Stars: The Challenge of Simplicity”. In: *Neutron Stars and Pulsars*. Ed. by Werner Becker. Berlin, Heidelberg: Springer Berlin Heidelberg, 2009, pp. 141–163. ISBN: 978-3-540-76965-1. DOI: `10.1007/978-3-540-76965-1_7`. URL: `https://doi.org/10.1007/978-3-540-76965-1_7`.

[18] Rim Dib, Victoria M. Kaspi, and Fotis P. Gavriil. “Glitches in Anomalous X-Ray Pulsars”. In: *The Astrophysical Journal* 673.2 (Feb. 2008), p. 1044. DOI: `10.1086/524653`. URL: `https://dx.doi.org/10.1086/524653`.

[19] Christopher Thompson and Robert C. Duncan. “Neutron Star Dynamos and the Origins of Pulsar Magnetism”. In: *Astrophysical Journal* 408 (May 1993), p. 194. DOI: `10.1086/172580`.

[20] Alaa I. Ibrahim et al. “Discovery of a Transient Magnetar: XTE J1810–197”. In: *The Astrophysical Journal* 609.1 (May 2004), p. L21. DOI: `10.1086/422636`. URL: `https://dx.doi.org/10.1086/422636`.

[21] N. Rea et al. “A Low-Magnetic-Field Soft Gamma Repeater”. In: *Science* 330.6006 (2010), pp. 944–946. DOI: `10.1126/science.1196088`. eprint: `https://www.science.org/doi/pdf/10.1126/science.1196088`. URL: `https://www.science.org/doi/abs/10.1126/science.1196088`.

[22] M. A. Livingstone, P. Scholz, V. M. Kaspi, C. Y. Ng, and Fotis P. Gavriil. "The spin-down of Swift J1822.3-1606: a new galactic magnetar". In: *The Astrophysical Journal Letters* 743.2 (2011). DOI: 10.1088/2041-8205/743/2/L38. URL: https://iopscience.iop.org/article/10.1088/2041-8205/743/2/L38.

[23] Andrea Tiengo et al. "A variable absorption feature in the X-ray spectrum of a magnetar". In: *Nature* (Aug. 2013). URL: https://doi.org/10.1038/nature12386.

[24] Michael P. Muno et al. "A Neutron Star with a Massive Progenitor in Westerlund 1". In: *The Astrophysical Journal* 636.1 (Dec. 2005). DOI: 10.1086/499776. URL: https://iopscience.iop.org/article/10.1086/499776.

[25] Lilia Ferrario and Dayal Wickramasinghe. "Origin and evolution of magnetars". In: *Monthly Notices of the Royal Astronomical Society: Letters* 389.1 (Sept. 2008), pp. L66–L70. ISSN: 1745-3925. DOI: 10.1111/j.1745-3933.2008.00527.x. eprint: https://academic.oup.com/mnrasl/article-pdf/389/1/L66/6379098/389-1-L66.pdf. URL: https://doi.org/10.1111/j.1745-3933.2008.00527.x.

[26] Todd A. Thompson, Philip Chang, and Eliot Quataert. "Magnetar Spin-Down, Hyperenergetic Supernovae, and Gamma-Ray Bursts". In: *The Astrophysical Journal* 611.1 (2004). DOI: 10.1086/421969. URL: https://iopscience.iop.org/article/10.1086/421969.

[27] Jacco Vink. "Supernova remnants with magnetars: Clues to magnetar formation". In: *Advances in Space Research* 41.3 (2008), pp. 503–511. ISSN: 0273-1177. DOI: https://doi.org/10.1016/j.asr.2007.06.042. URL: https://www.sciencedirect.com/science/article/pii/S0273117707006679.

[28] S. Dall'Osso, S. N. Shore, and L. Stella. "Early evolution of newly born magnetars with a strong toroidal field". In: *Monthly Notices of the Royal Astronomical Society* 398.4 (Sept. 2009), pp. 1869–1885. ISSN: 0035-8711. DOI: 10.1111/j.1365-2966.2008.14054.x. eprint: https://academic.oup.com/mnras/article-pdf/398/4/1869/3050465/mnras0398-1869.pdf. URL: https://doi.org/10.1111/j.1365-2966.2008.14054.x.

[29] A. I. Bogomazov and S. B. Popov. "Magnetars, gamma-ray bursts, and very close binaries". In: *Astronomy Reports* 53.4 (Apr. 2009), pp. 325–333. DOI: 10.1134/s1063772909040052. URL: https://doi.org/10.1134%2Fs1063772909040052.

[30] J. S. Clark, B. W. Ritchie, F. Najarro, N. Langer, and I. Negueruela. "A VLT/FLAMES survey for massive binaries in Westerlund 1". In: *Astronomy & Astrophysics* 565 (May 2014), A90. DOI: 10.1051/0004-6361/201321771. URL: https://doi.org/10.1051%2F0004-6361%2F201321771.

[31] Lilia Ferrario and Dayal Wickramasinghe. "Modelling of isolated radio pulsars and magnetars on the fossil field hypothesis". In: *Monthly Notices of the Royal Astronomical Society* 367.3 (Apr. 2006), pp. 1323–1328. ISSN: 0035-8711. DOI: 10.1111/j.1365-2966.2006.10058.x. eprint: https://academic.oup.com/mnras/article-pdf/367/3/1323/3528999/367-3-1323.pdf. URL: https://doi.org/10.1111/j.1365-2966.2006.10058.x.

[32] Lina Levin et al. "A radio-loud magnetar in X-ray Quiescence". In: *The Astrophysical Journal Letters* 721.1 (Aug. 2010). DOI: 10.1088/2041-8205/721/1/L33. URL: https://iopscience.iop.org/article/10.1088/2041-8205/721/1/L33.

[33] V. V. Uso. "Millisecond pulsars with extremely strong magnetic fields as a cosmological source of γ-ray bursts". In: *Nature* (June 1992). URL: https://doi.org/10.1038/357472a0.

[34] Bruno Giacomazzo and Rosalba Perna. "Formation of stable Magnetars from Binary Neutron Star Mergers". In: *The Astrophysical Journal Letters* 771.2 (June 2013), p. L26. DOI: 10.1088/2041-8205/771/2/L26. URL: https://dx.doi.org/10.1088/2041-8205/771/2/L26.

[35] K. Hurley et al. "An exceptionally bright flare from SGR 1806-20 and the origins of short-duration γ-ray bursts." In: *Nature* (May 2005). URL: https://doi.org/10.1038/nature03519.

[36] Geppert, U., Küker, M., and Page, D. "Temperature distribution in magnetized neutron star crusts - II. The effect of a strong toroidal component". In: *Astronomy & Astrophysics* 457.3 (2006), pp. 937–947. DOI: 10.1051/0004-6361:20054696. URL: https://doi.org/10.1051/0004-6361:20054696.

[37] Pons, J. A. and Geppert, U. "Magnetic field dissipation in neutron star crusts: from magnetars to isolated neutron stars". In: *Astronomy & Astrophysics* 470.1 (2007), pp. 303–315. DOI: 10.1051/0004-6361:20077456. URL: https://doi.org/10.1051/0004-6361:20077456.

[38] Peter Goldreich and Andreas Reisenegger. "Magnetic Field Decay in Isolated Neutron Stars". In: *The Astrophysical Journal* 395 (Aug. 1992), p. 250. DOI: 10.1086/171646.

[39] Alice K Harding and Dong Lai. "Physics of strongly magnetized neutron stars". In: *Reports on Progress in Physics* 69.9 (Aug. 2006), pp. 2631–2708. DOI: 10.1088/0034-4885/69/9/r03. URL: https://doi.org/10.1088%2F0034-4885%2F69%2F9%2Fr03.

[40] Andrew Cumming, Phil Arras, and Ellen Zweibel. "Magnetic Field Evolution in Neutron Star Crusts Due to the Hall Effect and Ohmic Decay". In: *The Astrophysical Journal* 609.2 (July 2004), pp. 999–1017. DOI: 10.1086/421324. URL: https://doi.org/10.1086%2F421324.

[41] Jungyeon Cho and A. Lazarian. "The Anisotropy of Electron Magnetohydrodynamic Turbulence". In: *The Astrophysical Journal* 615.1 (Sept. 2004), p. L41. DOI: 10.1086/425215. URL: https://dx.doi.org/10.1086/425215.

[42] P. Arras, A. Cumming, and C. Thompson. "Magnetars: Time Evolution, Superfluid Properties, and the Mechanism of Magnetic Field Decay". In: *The Astrophysical Journal* 608.1 (May 2004), p. L49. DOI: 10.1086/422337. URL: https://dx.doi.org/10.1086/422337.

[43] K. Glampedakis, D. I. Jones, and L. Samuelsson. "Ambipolar diffusion in superfluid neutron stars". In: *Monthly Notices of the Royal Astronomical Society* 413.3 (May 2011), pp. 2021–2030. ISSN: 0035-8711. DOI: 10.1111/j.1365-2966.2011.18278.x. eprint: https://academic.oup.com/mnras/article-pdf/413/3/2021/2894955/mnras0413-2021.pdf. URL: https://doi.org/10.1111/j.1365-2966.2011.18278.x.

[44] Davide De Grandis et al. “Three-dimensional Modeling of the Magnetothermal Evolution of Neutron Stars: Method and Test Cases”. In: *The Astrophysical Journal* 903.1 (Oct. 2020), p. 40. DOI: 10.3847/1538-4357/abb6f9. URL: https://doi.org/10.3847%2F1538-4357%2Fabb6f9.

[45] Christopher Thompson and Robert C. Duncan. “The Soft Gamma Repeaters as Very Strongly Magnetized Neutron Stars. II. Quiescent Neutrino, X-Ray, and Alfven Wave Emission”. In: *The Astrophysics Journal* 473 (Dec. 1996), p. 322. DOI: 10.1086/178147.

[46] Christopher Thompson and Robert C. Duncan. “The soft gamma repeaters as very strongly magnetized neutron stars - I. Radiative mechanism for outbursts”. In: *Monthly Notices of the Royal Astronomical Society* 275.2 (July 1995), pp. 255–300. DOI: 10.1093/mnras/275.2.255.

[47] Jonathan Braithwaite. “Axisymmetric magnetic fields in stars: relative strengths of poloidal and toroidal components”. In: *Monthly Notices of the Royal Astronomical Society* 397.2 (July 2009), pp. 763–774. ISSN: 0035-8711. DOI: 10.1111/j.1365-2966.2008.14034.x. eprint: https://academic.oup.com/mnras/article-pdf/397/2/763/2932157/mnras0397-0763.pdf. URL: https://doi.org/10.1111/j.1365-2966.2008.14034.x.

[48] Christopher Thompson et al. “Physical Mechanisms for the Variable Spin-down and Light Curve of SGR 1900+14”. In: *The Astrophysical Journal* 543.1 (Nov. 2000), p. 340. DOI: 10.1086/317072. URL: https://dx.doi.org/10.1086/317072.

[49] Andrei M. Beloborodov. “Untwisting Magnetospheres of Neutron Stars”. In: *The Astrophysical Journal* 703.1 (Sept. 2009). DOI: 10.1088/0004-637X/703/1/1044. URL: https://iopscience.iop.org/article/10.1088/0004-637X/703/1/1044.

[50] C. Thompson, M. Lyutikov, and S. R. Kulkarni. “Electrodynamics of Magnetars: Implications for the Persistent X-Ray Emission and Spin-down of the Soft Gamma Repeaters and Anomalous X-Ray Pulsars”. In: *The Astrophysical Journal* 574.1 (July 2002), pp. 332–355. DOI: 10.1086/340586. URL: https://doi.org/10.1086%2F340586.

[51] Andrei M. Beloborodov and Christopher Thompson. “Corona of Magnetars”. In: *The Astrophysical Journal* 657.2 (Mar. 2007), p. 967. DOI: 10.1086/508917. URL: https://dx.doi.org/10.1086/508917.

[52] Campana, S., Rea, N., Israel, G. L., Turolla, R., and Zane, S. “Swift and Chandra confirm the intensity-hardness correlation of the AXP 1RXS0849.0-400910”. In: *Astronomy & Astrophysics* 463.3 (2007), pp. 1047–1051. DOI: 10.1051/0004-6361:20065482. URL: https://doi.org/10.1051/0004-6361:20065482.

[53] L. Nobili, R. Turolla, and S. Zane. “X-ray spectra from magnetar candidates – I. Monte Carlo simulations in the non-relativistic regime”. In: *Monthly Notices of the Royal Astronomical Society* 386.3 (Apr. 2008), pp. 1527–1542. ISSN: 0035-8711. DOI: 10.1111/j.1365-2966.2008.13125.x. eprint: https://academic.oup.com/mnras/article-pdf/386/3/1527/3638288/mnras0386-1527.pdf. URL: https://doi.org/10.1111/j.1365-2966.2008.13125.x.

[54] Rodrigo Fernández and Christopher Thompson. "Resonant Cyclotron Scattering in Three Dimensions and the Quiescent Nonthermal X-ray Emission of Magnetars". In: *The Astrophysical Journal* 660.1 (May 2007), p. 615. DOI: `10.1086/511810`. URL: `https://dx.doi.org/10.1086/511810`.

[55] S. Bonazzola, J. Heyvaerts, and J. L. Puget. "Cyclotron line formation by resonant Compton-cyclotron scattering in Hercules X-1." In: *Astronomy and Astrophysics* 78 (Sept. 1979), pp. 53–64.

[56] A Yu Potekhin. "Atmospheres and radiating surfaces of neutron stars". In: *Physics-Uspekhi* 57.8 (Aug. 2014), pp. 735–770. DOI: `10.3367/ufne.0184.201408a.0793`. URL: `https://doi.org/10.3367%2Fufne.0184.201408a.0793`.

[57] Dong Lai and Edwin E. Salpeter. "Hydrogen Phases on the Surfaces of a Strongly Magnetized Neutron Star". In: *The Astrophysical Journal* 491.1 (Dec. 1997), p. 270. DOI: `10.1086/304937`. URL: `https://dx.doi.org/10.1086/304937`.

[58] Zach Medin and Dong Lai. "Condensed surfaces of magnetic neutron stars, thermal surface emission, and particle acceleration above pulsar polar caps". In: *Monthly Notices of the Royal Astronomical Society* 382.4 (Nov. 2007), pp. 1833–1852. ISSN: 0035-8711. DOI: `10.1111/j.1365-2966.2007.12492.x`. eprint: `https://academic.oup.com/mnras/article-pdf/382/4/1833/3957677/mnras0382-1833.pdf`. URL: `https://doi.org/10.1111/j.1365-2966.2007.12492.x`.

[59] Dong Lai. "Matter in strong magnetic fields". In: *Rev. Mod. Phys.* 73 (3 Aug. 2001), pp. 629–662. DOI: `10.1103/RevModPhys.73.629`. URL: `https://link.aps.org/doi/10.1103/RevModPhys.73.629`.

[60] S. A. Olausen and V. M. Kaspi. "The McGill Magnetar Catalog". In: *The Astrophysical Journal Supplement* 212.1, 6 (May 2014), p. 6. DOI: `10.1088/0067-0049/212/1/6`. arXiv: `1309.4167 [astro-ph.HE]`.

[61] J. P. Halpern and E. V. Gotthelf. "The Fading of Transient Anomalous X-Ray Pulsar XTE J1810-197". In: *The Astrophysical Journal* 618.2 (Jan. 2005), p. 874. DOI: `10.1086/426130`. URL: `https://dx.doi.org/10.1086/426130`.

[62] Aguilera, D. N., Pons, J. A., and Miralles, J. A. "2D Cooling of magnetized neutron stars". In: *Astronomy & Astrophysics* 486.1 (2008), pp. 255–271. DOI: `10.1051/0004-6361:20078786`. URL: `https://doi.org/10.1051/0004-6361:20078786`.

[63] Sandro Mereghetti, José A. Pons, and Andrew Melatos. "Magnetars: Properties, Origin and Evolution". In: *Space Science Reviews* 191.1-4 (Mar. 2015), pp. 315–338. DOI: `10.1007/s11214-015-0146-y`. URL: `https://doi.org/10.1007%2Fs11214-015-0146-y`.

[64] D. Marsden and N. E. White. "Correlations between Spectral Properties and Spin-down Rate in Soft Gamma-Ray Repeaters and Anomalous X-Ray Pulsars". In: 551.2 (Apr. 2001), p. L155. DOI: `10.1086/320025`. URL: `https://dx.doi.org/10.1086/320025`.

[65] S. Mereghetti et al. "An XMM-Newton View of the Soft Gamma Repeater SGR 1806-20: Long-Term Variability in the Pre-Giant Flare Epoch". In: *The Astrophysical Journal* 628.2 (Aug. 2005), p. 938. DOI: `10.1086/430943`. URL: `https://dx.doi.org/10.1086/430943`.

[66] A. Tiengo et al. "A phase-variable absorption feature in the X-ray spectrum of the magnetar SGR 0418+5729". In: *Astronomische Nachrichten* 335.3 (2014), pp. 274–279. ISSN: 0004-6337.

[67] Sandeep K. Patel et al. "Chandra Observations of the Anomalous X-Ray Pulsar 1E 2259+586". In: *The Astrophysical Journal* 563.1 (Nov. 2001), p. L45. DOI: 10.1086/338476. URL: https://dx.doi.org/10.1086/338476.

[68] N. Rea et al. "Very deep X-ray observations of the anomalous X-ray pulsar 4U 0142+614". In: *Monthly Notices of the Royal Astronomical Society* 381.1 (Sept. 2007), pp. 293–300. ISSN: 0035-8711. DOI: 10.1111/j.1365-2966.2007.12257.x. eprint: https://academic.oup.com/mnras/article-pdf/381/1/293/18572776/mnras0381-0293.pdf. URL: https://doi.org/10.1111/j.1365-2966.2007.12257.x.

[69] Teruaki Enoto et al. "Soft and Hard X-Ray Emissions from the Anomalous X-Ray Pulsar 4U 0142+61 Observed with Suzaku". In: *Publications of the Astronomical Society of Japan* 63.2 (Apr. 2011), pp. 387–396. ISSN: 0004-6264. DOI: 10.1093/pasj/63.2.387. eprint: https://academic.oup.com/pasj/article-pdf/63/2/387/17268459/pasj63-0387.pdf. URL: https://doi.org/10.1093/pasj/63.2.387.

[70] Mereghetti, S., Götz, D., Mirabel, I. F., and Hurley, K. "INTEGRAL discovery of persistent hard X-ray emission from the Soft Gamma-ray Repeater SGR 1806-20". In: *Astronomy & Astrophysics* 433.2 (2005), pp. L9–L12. DOI: 10.1051/0004-6361:200500088. URL: https://doi.org/10.1051/0004-6361:200500088.

[71] Götz, D., Mereghetti, S., Tiengo, A., and Esposito, P. "Magnetars as persistent hard X-ray sources: INTEGRAL discovery of a hard tail in SGR 1900+14". In: *Astronomy & Astrophysics* 449.2 (2006), pp. L31–L34. DOI: 10.1051/0004-6361:20064870. URL: https://doi.org/10.1051/0004-6361:20064870.

[72] V. M. Kaspi and K. Boydstun. "ON THE X-RAY SPECTRA OF ANOMALOUS X-RAY PULSARS AND SOFT GAMMA REPEATERS". In: *The Astrophysical Journal Letters* 710.2 (Jan. 2010), p. L115. DOI: 10.1088/2041-8205/710/2/L115. URL: https://dx.doi.org/10.1088/2041-8205/710/2/L115.

[73] Sinem Şaşmaz Muş and Ersin Göğüş. "Search for High-Energy Gamma-Ray Emission from an Anomalous X-Ray Pulsar, 4U 0142+61". In: 723.1 (Oct. 2010), p. 100. DOI: 10.1088/0004-637X/723/1/100. URL: https://dx.doi.org/10.1088/0004-637X/723/1/100.

[74] E. P. Mazets, S. V. Golenetskij, and Y. A. Guryan. "Soft gamma-ray bursts from the source B1900+14". In: *Soviet Astronomy Letters* 5 (Dec. 1979), p. 343.

[75] V. M. Kaspi et al. "A Major Soft Gamma Repeater-like Outburst and Rotation Glitch in the No-longer-so-anomalous X-Ray Pulsar 1E 2259+586". In: *The Astrophysical Journal* 588.2 (Apr. 2003), p. L93. DOI: 10.1086/375683. URL: https://dx.doi.org/10.1086/375683.

[76] Rim Dib and Victoria M. Kaspi. "16 yr of RXTE Monitoring of five Anomalous X-Ray Pulsars". In: *The Astrophysical Journal* 784.1 (Mar. 2014), p. 37. DOI: 10.1088/0004-637X/784/1/37. URL: https://dx.doi.org/10.1088/0004-637X/784/1/37.

[77] P. Scholz, V. M. Kaspi, and A. Cumming. “The Long-Term Post-Outburst Spin Down and Flux Relaxation of Magnetar SWIFT J1822.3-1606”. In: *The Astrophysical Journal* 786.1 (Apr. 2014), p. 62. DOI: `10.1088/0004-637X/786/1/62`. URL: `https://dx.doi.org/10.1088/0004-637X/786/1/62`.

[78] N. Rea et al. “A Low-Magnetic-Field Soft Gamma Repeater”. In: *Science* 330.6006 (2010), pp. 944–946. DOI: `10.1126/science.1196088`. eprint: `https://www.science.org/doi/pdf/10.1126/science.1196088`. URL: `https://www.science.org/doi/abs/10.1126/science.1196088`.

[79] Lin Lin, Ersin Göğüş, Yuki Kaneko, and Chryssa Kouveliotou. “DETAILED INVESTIGATIONS OF THE DIMMEST BURSTS FROM TWO MAGNETARS, SGR J0501+4516 AND SGR J1550−5418”. In: *The Astrophysical Journal* 778.2 (Nov. 2013), p. 105. DOI: `10.1088/0004-637X/778/2/105`. URL: `https://dx.doi.org/10.1088/0004-637X/778/2/105`.

[80] Harsha S. Kumar, Alaa I. Ibrahim, and Samar Safi-Harb. “SWIFT-BAT OBSERVATIONS OF THE RECENTLY DISCOVERED MAGNETAR SGR 0501+4516”. In: *The Astrophysical Journal* 716.1 (May 2010), p. 97. DOI: `10.1088/0004-637X/716/1/97`. URL: `https://dx.doi.org/10.1088/0004-637X/716/1/97`.

[81] Hongjun An et al. “NuSTAR OBSERVATIONS OF X-RAY BURSTS FROM THE MAGNETAR 1E 1048.1−5937”. In: *The Astrophysical Journal* 790.1 (July 2014), p. 60. DOI: `10.1088/0004-637X/790/1/60`. URL: `https://dx.doi.org/10.1088/0004-637X/790/1/60`.

[82] Ersin Göğüş et al. “Statistical Properties of SGR 1900+14 Bursts”. In: *The Astrophysical Journal* 526.2 (Oct. 1999), p. L93. DOI: `10.1086/312380`. URL: `https://dx.doi.org/10.1086/312380`.

[83] Fotis P. Gavriil, Victoria M. Kaspi, and Peter M. Woods. “A Comprehensive Study of the X-Ray Bursts from the Magnetar Candidate 1E 2259+586”. In: *The Astrophysical Journal* 607.2 (June 2004), p. 959. DOI: `10.1086/383564`. URL: `https://dx.doi.org/10.1086/383564`.

[84] Alaa I. Ibrahim et al. “An Unusual Burst from Soft Gamma Repeater SGR 1900+14: Comparisons with Giant Flares and Implications for the Magnetar Model”. In: *The Astrophysical Journal* 558.1 (Sept. 2001), p. 237. DOI: `10.1086/322248`. URL: `https://dx.doi.org/10.1086/322248`.

[85] G. L. Israel et al. “A Swift Gaze into the 2006 March 29 Burst Forest of SGR 1900+14”. In: *The Astrophysical Journal* 685.2 (Oct. 2008), p. 1114. DOI: `10.1086/590486`. URL: `https://dx.doi.org/10.1086/590486`.

[86] E. E. Fenimore, R. W. Klebesadel, and J. G. Laros. “The 1979 March 5 Gamma-Ray Transient: Was It a Classic Gamma-Ray Burst?” In: *The Astrophysical Journal* 460 (Apr. 1996), p. 964. DOI: `10.1086/177024`. arXiv: `astro-ph/9509142 [astro-ph]`.

[87] M. Feroci, K. Hurley, R. C. Duncan, and C. Thompson. “The Giant Flare of 1998 August 27 from SGR 1900+14. I. An Interpretive Study of BeppoSAX and Ulysses Observations”. In: *The Astrophysical Journal* 549.2 (Mar. 2001), p. 1021. DOI: `10.1086/319441`. URL: `https://dx.doi.org/10.1086/319441`.

[88] D. M. Palmer et al. “A giant γ-ray flare from the magnetar SGR 1806−20”. In: *Nature* (Apr. 2005). URL: `https://doi.org/10.1038/nature03525`.

[89] K. Hurley et al. “An exceptionally bright flare from SGR 1806−20 and the origins of short-duration γ-ray bursts”. In: *Nature* (Apr. 2005). URL: https://doi.org/10.1038/nature03519.

[90] F. Camilo et al. “Transient pulsed radio emission from a magnetar”. In: *Nature* (Aug. 2006). URL: https://doi.org/10.1038/nature04986.

[91] Lina Levin et al. “A RADIO-LOUD MAGNETAR IN X-RAY QUIESCENCE”. In: *The Astrophysical Journal Letters* 721.1 (Aug. 2010), p. L33. DOI: 10.1088/2041-8205/721/1/L33. URL: https://dx.doi.org/10.1088/2041-8205/721/1/L33.

[92] Nanda Rea, José A. Pons, Diego F. Torres, and Roberto Turolla. “THE FUNDAMENTAL PLANE FOR RADIO MAGNETARS”. In: *The Astrophysical Journal Letters* 748.1 (Feb. 2012), p. L12. DOI: 10.1088/2041-8205/748/1/L12. URL: https://dx.doi.org/10.1088/2041-8205/748/1/L12.

[93] Wynn C. G. Ho. “More than meets the eye: magnetars in disguise”. In: *Monthly Notices of the Royal Astronomical Society* 429.1 (Nov. 2012), pp. 113–118. ISSN: 0035-8711. DOI: 10.1093/mnras/sts317. eprint: https://academic.oup.com/mnras/article-pdf/429/1/113/3319148/sts317.pdf. URL: https://doi.org/10.1093/mnras/sts317.

[94] D. A. Frail, S. R. Kulkarni, and J. S. Bloom. “An outburst of relativistic particles from the soft γ-ray repeater SGR1900+14”. In: *Nature* (Mar. 1999). URL: https://doi.org/10.1038/18163.

[95] R. P. Fender et al. “Structure in the radio counterpart to the 2004 December 27 giant flare from SGR 1806–20”. In: *Monthly Notices of the Royal Astronomical Society: Letters* 367.1 (Mar. 2006), pp. L6–L10. ISSN: 1745-3925. DOI: 10.1111/j.1745-3933.2006.00123.x. eprint: https://academic.oup.com/mnrasl/article-pdf/367/1/L6/4032986/367-1-L6.pdf. URL: https://doi.org/10.1111/j.1745-3933.2006.00123.x.

[96] Yuri Lyubarsky. “A model for fast extragalactic radio bursts”. In: *Monthly Notices of the Royal Astronomical Society: Letters* 442.1 (Apr. 2014), pp. L9–L13. ISSN: 1745-3925. DOI: 10.1093/mnrasl/slu046. eprint: https://academic.oup.com/mnrasl/article-pdf/442/1/L9/9371140/slu046.pdf. URL: https://doi.org/10.1093/mnrasl/slu046.

[97] F. Y. Wang, G. Q. Zhang, Z. G. Dai, and K. S. Cheng. “Repeating fast radio burst 20201124A originates from a magnetar/Be star binary”. In: *Nature Communications* 13.1 (Sept. 2022). DOI: 10.1038/s41467-022-31923-y. URL: https://doi.org/10.1038%2Fs41467-022-31923-y.

[98] Martin Durant and Marten H. van Kerkwijk. “Extinction Columns and Intrinsic X-Ray Spectra of the Anomalous X-Ray Pulsars”. In: *The Astrophysical Journal* 650.2 (Oct. 2006), p. 1082. DOI: 10.1086/507174. URL: https://dx.doi.org/10.1086/507174.

[99] V. S. Dhillon et al. “The first observation of optical pulsations from a soft gamma repeater: SGR 0501+4516”. In: *Monthly Notices of the Royal Astronomical Society: Letters* 416.1 (Sept. 2011), pp. L16–L20. ISSN: 1745-3925. DOI: 10.1111/j.1745-3933.2011.01088.x. eprint: https://academic.oup.com/mnrasl/article-pdf/416/1/L16/6141126/416-1-L16.pdf. URL: https://doi.org/10.1111/j.1745-3933.2011.01088.x.

[100] Z. Wang, D. Chakrabarty, and David L. Kaplan. “A debris disk around an isolated young neutron star”. In: *Nature* (Apr. 2006). URL: https://doi.org/10.1038/nature04669.

[101] Sergio Fabiani and Fabio Muleri. *Astronomical X-Ray polarimetry.* Aracne, 2014, p. 204.

[102] R. Taverna et al. “Polarization of neutron star surface emission: a systematic analysis”. In: *Monthly Notices of the Royal Astronomical Society* 454.3 (Oct. 2015), pp. 3254–3266. ISSN: 0035-8711. DOI: 10.1093/mnras/stv2168. eprint: https://academic.oup.com/mnras/article-pdf/454/3/3254/4039130/stv2168.pdf. URL: https://doi.org/10.1093/mnras/stv2168.

[103] Yu. N. Gnedin and G. G. Pavlov. “The transfer equations for normal waves and radiation polarization in an anisotropic medium”. In: *Journal of Experimental and Theoretical Physics* 38.5 (May 1974). URL: http://jetp.ras.ru/cgi-bin/e/index/e/38/5/p903?a=list.

[104] Rodrigo Fernández and Shane W. Davis. “THE X-RAY POLARIZATION SIGNATURE OF QUIESCENT MAGNETARS: EFFECT OF MAGNETOSPHERIC SCATTERING AND VACUUM POLARIZATION”. In: *The Astrophysical Journal* 730.2 (Mar. 2011), p. 131. DOI: 10.1088/0004-637X/730/2/131. URL: https://dx.doi.org/10.1088/0004-637X/730/2/131.

[105] Jeremy S. Heyl and Nir J. Shaviv. “Polarization evolution in strong magnetic fields”. In: *Monthly Notices of the Royal Astronomical Society* 311.3 (Jan. 2000), pp. 555–564. DOI: 10.1046/j.1365-8711.2000.03076.x. arXiv: astro-ph/9909339 [astro-ph].

[106] Dong Lai and Wynn C. Ho. “Polarized X-Ray Emission from Magnetized Neutron Stars: Signature of Strong-Field Vacuum Polarization”. In: *Physical Review Letters* 91.7, 071101 (Aug. 2003), p. 071101. DOI: 10.1103/PhysRevLett.91.071101. arXiv: astro-ph/0303596 [astro-ph].

[107] Dong Lai and Wynn C. G. Ho. “Transfer of Polarized Radiation in Strongly Magnetized Plasmas and Thermal Emission from Magnetars: Effect of Vacuum Polarization”. In: *The Astrophysical Journal* 588.2 (May 2003), pp. 962–974. DOI: 10.1086/374334. arXiv: astro-ph/0211315 [astro-ph].

[108] Akihiro Yatabe and Shoichi Yamada. “Systematic Analysis of the Effects of Mode Conversion on Thermal Radiation from Neutron Stars”. In: *The Astrophysical Journal* 850.2 (Dec. 2017), p. 185. DOI: 10.3847/1538-4357/aa97d8. URL: https://dx.doi.org/10.3847/1538-4357/aa97d8.

[109] Wynn C. G. Ho and Dong Lai. “Spectral Features in the Thermal Emission from Isolated Neutron Stars: Dependence on Magnetic Field Strengths”. In: *The Astrophysical Journal* 607.1 (May 2004), p. 420. DOI: 10.1086/383341. URL: https://dx.doi.org/10.1086/383341.

[110] C. Sgrò. “The Imaging X-ray Polarimetry Explorer (IXPE)”. In: *Nuclear Instruments and Methods in Physics Research Section A: Accelerators, Spectrometers, Detectors and Associated Equipment* 936 (2019). Frontier Detectors for Frontier Physics: 14th Pisa Meeting on Advanced Detectors, pp. 212–215. ISSN: 0168-9002. DOI: https://doi.org/10.1016/j.nima.2018.10.111. URL: https://www.sciencedirect.com/science/article/pii/S0168900218314268.

[111] Martin C. Weisskopf et al. “The Imaging X-ray Polarimetry Explorer (IXPE)”. In: *Results in Physics* 6 (2016), pp. 1179–1180. ISSN: 2211-3797. DOI: https://doi.org/10.1016/j.rinp.2016.10.021. URL: https://www.sciencedirect.com/science/article/pii/S221137971630448X.

[112] Brian D. Ramsey et al. “IXPE mirror module assemblies”. In: 11119 (2020). Ed. by Stephen L. O’Dell and Giovanni Pareschi, p. 1111903. DOI: 10.1117/12.2531956. URL: https://doi.org/10.1117/12.2531956.

[113] Paolo Soffitta et al. “The Instrument of the Imaging X-Ray Polarimetry Explorer”. In: *The Astronomical Journal* 162.5 (Oct. 2021), p. 208. DOI: 10.3847/1538-3881/ac19b0. URL: https://dx.doi.org/10.3847/1538-3881/ac19b0.

[114] Enrico Costa et al. “An efficient photoelectric X-ray polarimeter for the study of black holes and neutron stars”. In: *Nature* 411.6838 (June 2001), pp. 662–665. DOI: 10.1038/35079508. URL: https://doi.org/10.1038%2F35079508.

[115] Luca Baldini et al. “ixpeobssim: A simulation and analysis framework for the imaging X-ray polarimetry explorer”. In: *SoftwareX* 19 (July 2022), p. 101194. DOI: 10.1016/j.softx.2022.101194. URL: https://doi.org/10.1016%2Fj.softx.2022.101194.

[116] Martin C. Weisskopf, Ronald F. Elsner, and Stephen L. O’Dell. “On understanding the figures of merit for detection and measurement of x-ray polarization”. In: (July 2010). Ed. by Monique Arnaud, Stephen S. Murray, and Tadayuki Takahashi. DOI: 10.1117/12.857357. URL: https://doi.org/10.1117%2F12.857357.

[117] P. A. Connors, T. Piran, and R. F. Stark. “Polarization features of X-ray radiation emitted near black holes.” In: *Astrophysical Journal* 235 (Jan. 1980), pp. 224–244. DOI: 10.1086/157627.

[118] Roberto Turolla et al. *IXPE and XMM-Newton observations of the Soft Gamma Repeater SGR 1806-20*. 2023. arXiv: 2308.01238 [astro-ph.HE].

[119] Silvia Zane et al. “A Strong X-Ray Polarization Signal from the Magnetar 1RXS J170849.0-400910”. In: *The Astrophysical Journal Letters* 944.2 (Feb. 2023), p. L27. DOI: 10.3847/2041-8213/acb703. URL: https://dx.doi.org/10.3847/2041-8213/acb703.